11/21/2000

ELECTROMAGNETIC ELECTRON AND PROTON CYCLOTRON WAVES IN GEOSPACE: A CASSINI SNAPSHOT

B. T. Tsurutani, J. K. Arballo, C. Galvan, and X.-Y. Zhou

Jet Propulsion Laboratory, California Institute of Technology, 4800 Oak Grove Drive, Pasadena, CA 91109, USA

ABSTRACT

The Cassini spacecraft flew past the Earth in a trajectory almost along the Sun-Earth line, giving a unique perspective of low frequency waves in geospace. Geotail was immediately upstream of the bow shock nose, allowing for an accurate assessment of the solar wind conditions driving geospace macroscale processes, the latter of which led to microinstabilities and electromagnetic plasma wave growth. We demonstrate the presence of nonlinear cyclotron waves in the foreshock, magnetosheath and outer magnetosphere. Wave modes previously unidentified have been detected in the north tail lobe during substorms. A predominance of right-hand cyclotron waves with $f = 1.25$ Hz (in the spacecraft frame) are detected in the foreshock. The waves are compressional with $\Delta\vec{B}/B$ ~0.25. It is argued that these waves are propagating in the electron cyclotron (magnetosonic) mode and that the waves are locally generated by electrons streaming into the upstream region with parallel kinetic energies of ~6.5 keV. This region appears to be a pure electron foreshock. The magnetosheath waves are the largest amplitude (~15 nT peak-to-peak in a ~30 nT field) proton cyclotron waves detected in geospace. The wave amplitudes are largest near the bow shock and decrease to ~8 nT peak-to-peak near the magnetopause. No discernible mirror mode structures were detected in the magnetosheath. It is speculated that a low abundance of He^{++} ions in the solar wind high-speed stream may be the cause of the ion cyclotron wave dominance, as previously predicted by theory.

The outer magnetospheric proton cyclotron waves are of low intensity (~4 nT peak-to-peak), and can cause weak proton pitch angle diffusion and concomitant diffuse proton aurora. Large-scale solar wind ram pressure pulses do not appear to be the cause of the magnetospheric waves. However, small scale fluctuations are possible. Two new low-intensity wave modes are identified in the tail lobes associated with substorm events. One mode is a transverse, elliptically polarized ~7.5 s wave and the other is a purely compressional (~0.1 nT amplitude) wave, with an ~8 s quasiperiod. The latter mode is propagating obliquely (70° to 84°) to the magnetic field.

INTRODUCTION

The Cassini spacecraft had a unique trajectory in its flyby past the Earth on 18 August 1999. Cassini had a path through the subsolar point of the Earth's foreshock and magnetosheath and then flew through the magnetosphere and down the north lobe of the magnetotail. Cassini exited the dawnside of the magnetotail at $X \approx -70\ R_e$. This flyby took a total time of ~10 hours, thus one can get a unique "snapshot"

of low frequency plasma waves in the near-Earth environment. What was particularly striking was that much of this interval was filled with intense, nonlinear electromagnetic plasma waves.

The solar wind interaction with the magnetosphere/magnetotail influences all of geospace, and thus the solar wind is the ultimate source of local plasma instabilities and concomitant wave growth. It was particularly fortunate, during the Cassini flyby, to have the GEOTAIL spacecraft positioned just upstream of the bow shock nose so that it could serve as an upstream monitor. ACE was located farther upstream of the Earth, near the L_1 libration point. Solar wind ram pressure variations lead to magnetosheath/outer magnetosphere/near-Earth magnetotail compressions and rarefractions, and the embedded interplanetary B_S magnetic fields can lead to magnetic reconnection and substorms (Dungey, 1961). Solar wind velocity and magnetic field directional variations can result in bow shock strength and shock Mach number fluctuations (Kennel *et al.*, 1985). These large scale processes in turn cause microscale processes and plasma instabilities, the topic of this paper.

The Earth's foreshock is typically dominated by low frequency (10 to 60 s periods) electromagnetic plasma waves occurring in the foreshock (Fairfield, 1969; Hoppe *et al.*, 1981). The waves are associated with energetic ion beams streaming into the upstream medium (Asbridge *et al.*, 1968; Thomsen, 1985, and references therein), and are believed to be generated by an ion-ion instability (Papadopoulos, 1985; Gary, 1991). However, it has been argued that the particle source may be either bow-shock reflected solar wind ions (Bonifazi and Moreno, 1981a,b), escaping magnetospheric ions (Baker *et al.*, 1988; Sibeck *et al.*, 1988), or possibly even energetic electrons (Smith *et al.*, 1976; Goldstein *et al.*, 1985). Foreshock/shock particle energization processes can occur through interaction with the waves through either Fermi (Lee, 1982; Forman and Webb, 1985) and/or gradient B drift shock (Armstrong *et al.*, 1985) acceleration. The Earth's magnetosheath is typically dominated by nonoscillatory mirror mode structures (Tsurutani *et al.*, 1982; Anderson *et al.*, 1994), even though the ion cyclotron mode theoretically has higher growth rates (Price *et al.*, 1986). Gary *et al.* (1992), in agreement with the work of Price *et al.* (1986), explained the dominance of mirror mode structures in the magnetosheath as being due to the presence of small amounts of He^{++} in the solar wind and magnetosheath (see also Brinca and Tsurutani, 1989). In this scenario, the He^{++} ions create a stop-band in the proton cyclotron dispersion relationship, effectively reducing the proton cyclotron wave growth rate. Proton cyclotron waves have been detected

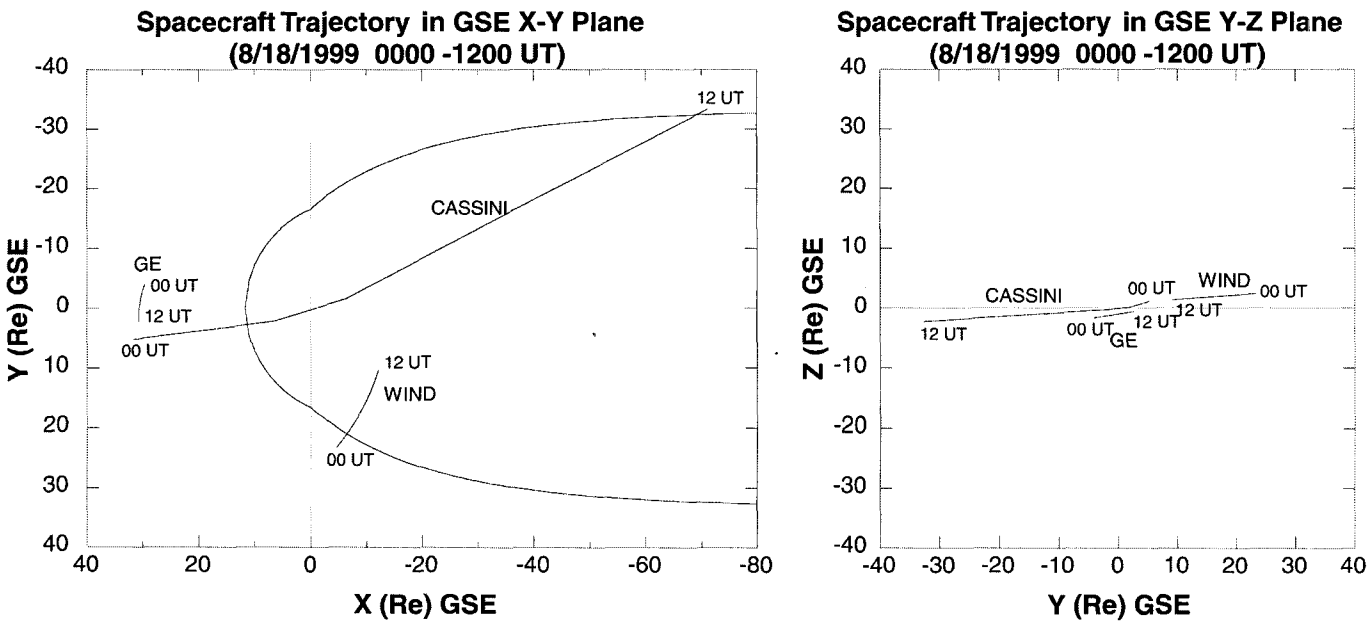

Fig. 1. Trajectories of Cassini, WIND, and GEOTAIL during the Cassini Earth flyby, in GSE coordinates.

in the outer magnetosphere during solar wind compression events (Anderson and Hamilton, 1993). The waves are generated by a proton temperature anisotropy ($T_\perp/T_\parallel > 1$) instability, the latter which results presumably from adiabatic compression of preexisting energetic protons in the outer magnetosphere. Low frequency electromagnetic waves in the tail (Tsurutani and Smith, 1984) have been ascribed as being due to generation by ion beams streaming away from the tail reconnection *X*-line (Cowley *et al.*, 1984; Tsurutani *et al.*, 1985) in the low beta plasmasheet boundary layer. This instability has been discussed in detail by Gary *et al.* (1985).

The purpose of this paper is to analyze and characterize the low frequency electromagnetic plasma waves in the four regions of geospace (foreshock, magnetosheath, outer magnetosphere and near-Earth magnetotail lobe), and to determine the solar wind influence (or lack of it) on waves in each region. We will demonstrate that the macroscale properties of the solar wind have significant influence on the wave modes and intensities for these various regions of geospace.

RESULTS

Wave Overview

The Cassini encounter trajectory is shown in Figure 1. The left-hand panel shows the trajectory projected into the GSE X-Y plane and the right-hand panel, the trajectory projected into the GSE Y-Z plane. In this coordinate system $\hat{x}$ is in the Earth-Sun direction, $\hat{y}$ is in the plane of the ecliptic in the direction of motion opposite to the Earth's rotation about the Sun, and $\hat{z}$ forms the right-hand system. The Petrinec and Russell (1996) magnetospheric shape is shown as a reference. Cassini enters the magneto-sheath/magnetosphere essentially along the Sun-Earth line.

The figure also shows the trajectories of two other spacecraft: GEOTAIL (designated by GE), and WIND. GEOTAIL is positioned ~20 R_e upstream of the magnetopause nose, an ideal position to monitor the solar wind conditions and their variations during the encounter. In the figure, WIND starts (at 0000 UT) in the solar wind, then enters the magnetosheath shortly thereafter. Not shown is the ACE spacecraft which is orbiting the L_1 libration point. ACE was at 248, –4, 24 R_e.

An overview of the Cassini foreshock and magnetosheath waves is shown in Figure 2. The upstream interplanetary magnetic field (for reference, the bow shock is located at ~0151:50 UT) is (B_x, B_y, B_z) = –3, +3, –8 nT, in GSM coordinates. In this system, $\hat{x}$ is in the direction from the Earth to the Sun, $\hat{y} = \hat{x} \times \hat{M} / |\hat{x} \times \hat{M}|$, where $\hat{M}$ is the south magnetic dipole direction, and $\hat{z}$ completes the right-hand system. The interplanetary field is a positive sector field with a strongly negative B_z component. The magnetic field has an orientation ~70° relative to the Sun-Earth line.

Both the B_y and B_z components are intensified at and behind the bow shock (~0151:50 UT). The magnitude of the magnetic field increases from ~8 nT upstream (B_1) to ~32 nT downstream (B_2). The ratio $B_2/B_1 \approx 4.0$, the maximum expected for MHD shocks (Kennel et al., 1985). There is a significant shock "overshoot", where the field reaches ~47 nT. "Overshoots" are typically associated with ion deflection at supercritical shocks (Goodrich, 1985).

At 0148 UT at GEOTAIL (Figure 3), the solar wind velocity was ~560 km s^{-1}, density 3 cm^{-3}, thermal energy 20 eV and magnetic field strength 8.5 nT. The Alfvén speed $\left(B^2/4\pi\rho\right)^{1/2}$ was therefore 107 km s^{-1}, sound speed $(\gamma P/\rho)^{1/2}$ ~58 km s^{-1}, and magnetosonic speed 121 km s^{-1}. The ion cyclotron, electron cyclotron and electron plasma frequencies were 1.5 x 10^{-1} Hz, 2.3 x 10^2 Hz and 1.5 x 10^4 Hz,

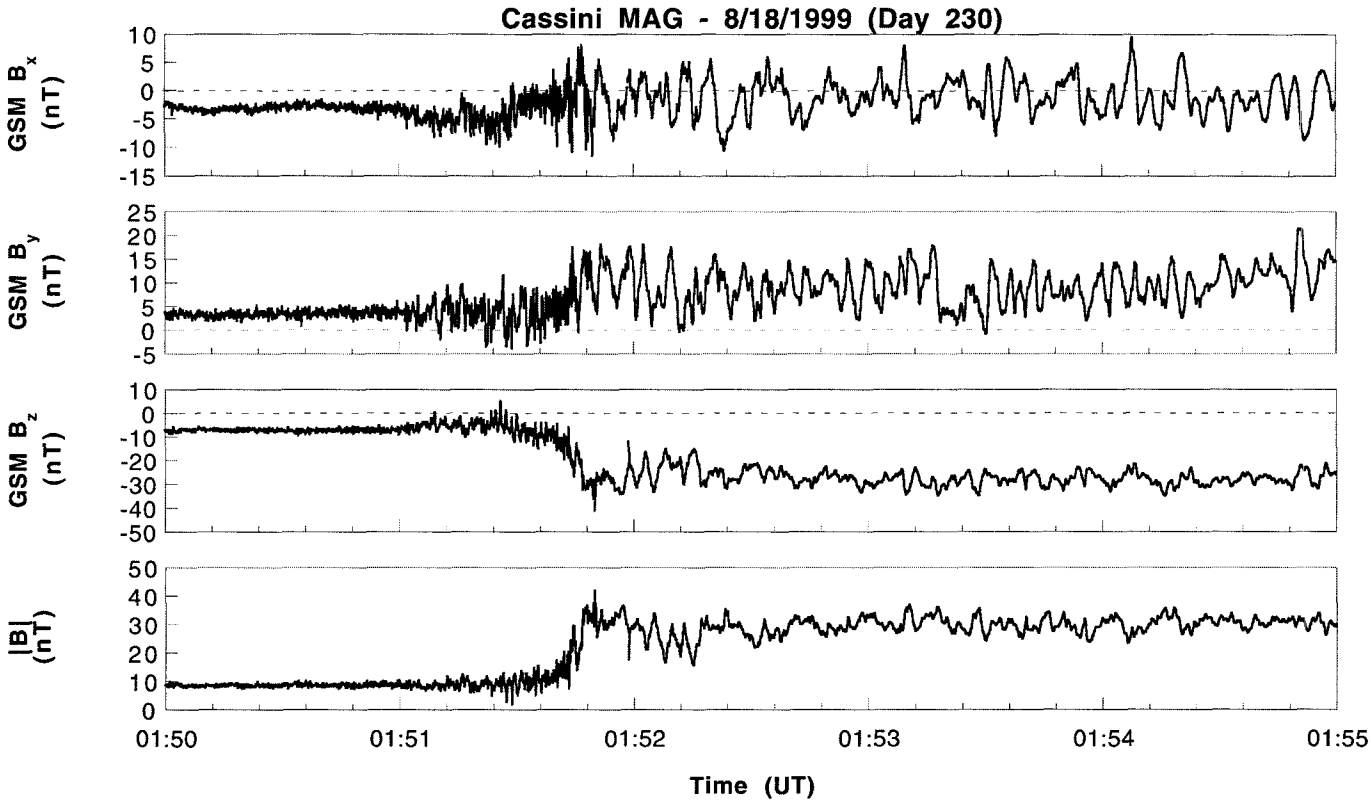

Fig. 2. The Earth's foreshock and magnetosheath waves detected by Cassini. The bow shock is located at ~0151:50 UT.

respectively. From magnetic coplanetary analyses, the shock normal was determined to be $\theta_{Bn} = 63°$, oriented at (0.96, –0.29, –0.04) in GSE coordinates. The shock magnetosonic Mach number was ~4.6.

Upstream of the shock (Figure 2), foreshock waves had higher frequencies (in the spacecraft frame) than the downstream magnetosheath waves. The foreshock wave amplitudes were largest nearest the shock, and they decreased with increasing upstream distance. This amplitude falloff is consistent with the free energy for wave growth being largest near the shock and decreasing with increasing distance (consistent with a shock-reflected particle beam or magnetospheric particle escape mechanism).

The post-shock magnetosheath waves were of lower frequency, beginning directly at the shock and continuing into the downstream region to the magnetopause (not shown in this figure). In Figure 2, the waves are noted to be quasiperiodic and are exceptionally large in amplitude. Immediately behind the shock, the waves have ~15 nT peak-to-peak amplitudes in a ~30 nT field.

Figure 4 shows the full sheath, up to and past the magnetopause (located at ~0226 UT). The magnetic field magnitude slowly increased from the post-shock region (~32 nT as previously stated), to ~60 nT just prior to the magnetopause. B_y increased from ~10 nT to ~30 nT and B_z from ~ –30 nT to ~ –55 nT during the same time interval of time. This steady magnetic field magnitude increase with decreasing distance from the magnetopause is due to the Zwan-Wolf (1976) field draping effect, where magnetosheath magnetic fields "drape" around the magnetosphere. As the magnetosheath plasma and fields are convected towards the stagnation point (the magnetopause nose), more and more plasma gets squeezed out the ends of the flux tubes leading to higher magnetic field strengths and lower plasma densities (lower plasma betas) near the magnetopause. This general trend can be noted in the figure.

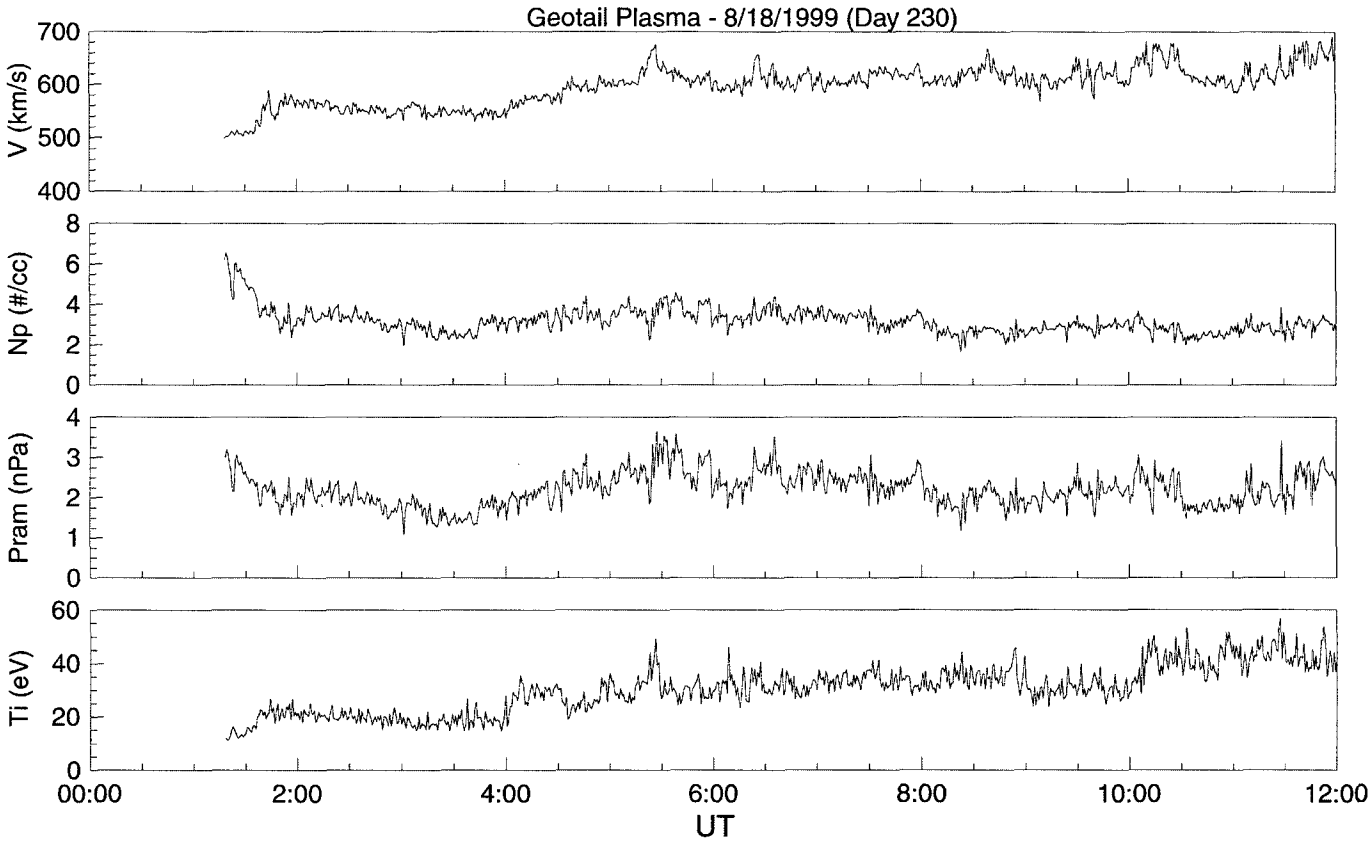

Fig. 3. The upstream solar wind during the time of the Cassini Earth-encounter.

Although the wave amplitudes were large throughout the magnetosheath, they gradually decreased from the bow shock to the magnetopause. This can be noted in the B_x component, the component most transverse to the ambient field direction. Another feature of the waves is that they were generally noncompressive. The largest field magnitude variations were present at ~0215 UT with ~6 nT magnitude variations in a ~40 nT field. These decreases were quite small compared to the typical 50 - 80% variations typical of mirror mode structures (Tsurutani et al., 1982).

Magnetopause

The minimum variance analysis results of the magnetopause are shown in Figure 5. The analysis was performed on 32 vector per second fields, the highest time resolution available for the Cassini magnetometer (Dougherty, et al., 1999). The magnetopause current layer is quite broad, extending from 0225:44 UT to 0226:05 UT. There is a large, steady normal field component (B_3) of ~8 nT present. The large normal component indicates that this is a rotational discontinuity (Sonnerup and Ledley, 1974), consistent with the concept that magnetic reconnection is taking place at this boundary (the magnetopause).

Solar Wind Overview

Before going into a detailed discussion of the LF plasma waves, the solar wind plasma and field conditions should be discussed. Both the general state and variations of this interplanetary driver can have significant impact on the magnetosphere interaction, as we will show later.

Figure 3 showed the GEOTAIL solar wind plasma parameters for the Cassini encounter interval (there was a spacecraft tracking gap from 0000 to ~0120 UT but this is not important for this study). The

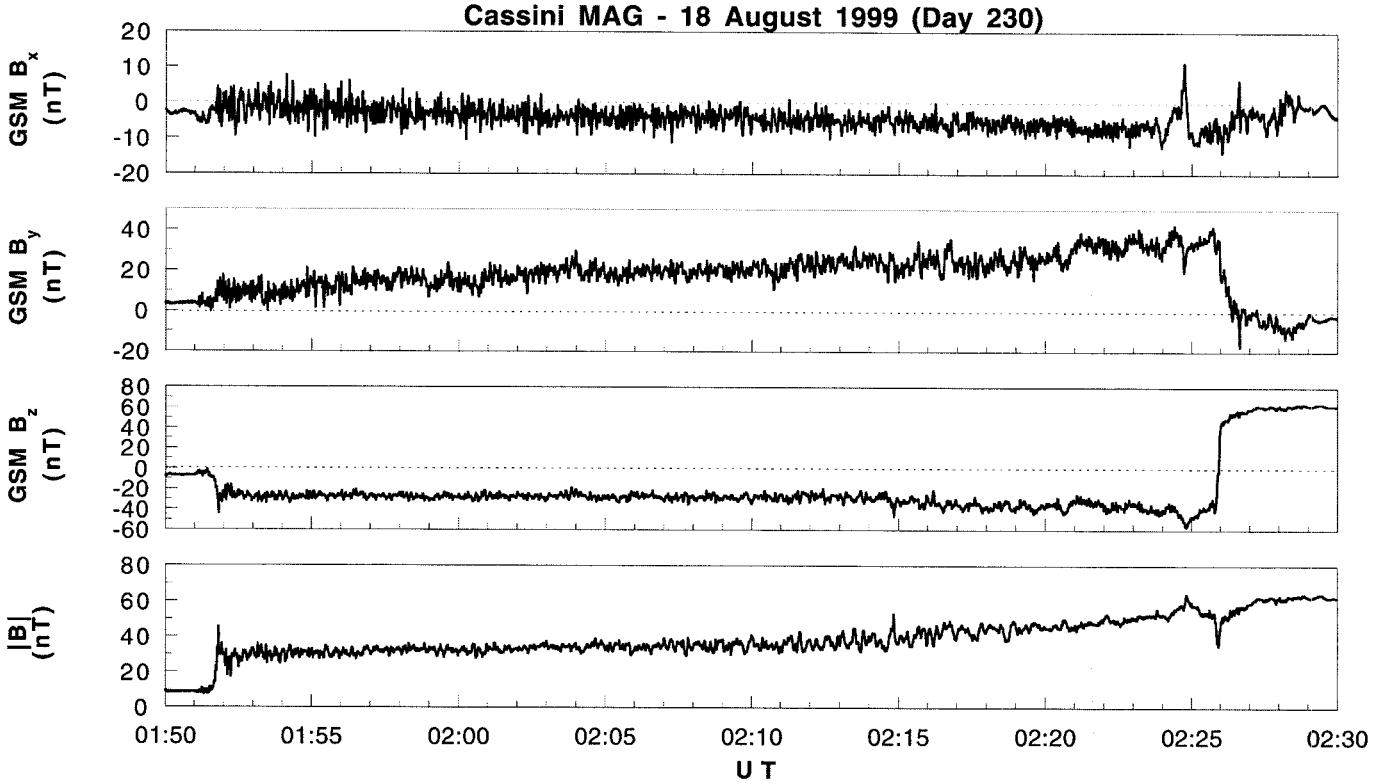

Fig. 4. The magnetosheath magnetic fields and superposed waves.

foreshock wave data interval (Figure 2) started at ~0150 UT. The solar wind speed is given in the top panel of the figure. The speed gradually increased from ~500 km s^{-1} to ~680 km s^{-1} over the ~10 hour Cassini interval.

Coincident with this solar velocity increase was a decrease in proton density. The proton density was ~6.0 cm^{-3} at 0120 UT and decreased to ~3.0 cm^{-3} by 1200 UT. The proton thermal energy increased from ~10 eV to ~45 eV in the same time interval. The variation of the three parameters indicates that GEOTAIL (and the Earth) were becoming engulfed in a high-speed (coronal hole) stream (Phillips et al., 1994). This general scenario has been verified using the ACE plasma data. A peak velocity of ~800 km s^{-1}, minimum plasma density of ~2.0 cm^{-3}, and peak proton thermal energy of ~50 eV was attained at ~1200 UT day 231 (one day later, not shown). One property of high-speed streams is that the He^{++} content has an average of 4.4% with "small" variations from the average (McComas et al., 1996). On the other hand, the He^{++} fractional density varies greatly in the slow solar wind (with averages of ~4%) and can be highest (>10%) in ICMEs.

The third panel in Figure 5 gives the solar wind ram pressure. This has been calculated assuming 4% He^{++} ions. The He^{++} measurements were unfortunately not available from GEOTAIL (He^{++} is not being standardly reduced. T. Mukai, personal communication, 2000). During the Cassini encounter, GEOTAIL was located ~20 R_e upstream of the Earth's magnetopause (assumed to be located at $x = 10$ R_e). The solar wind, with a speed of ~560 km s^{-1}, would take ~4 min. to convect from GEOTAIL to the magnetopause (this propagation time has been taken out for the purposes of the following discussion). During the foreshock traversal (~0151:00 to ~0151:50 UT), the solar wind ram pressure was more or less constant, with some small variations. During the first portion of the magnetosheath traversal, the ram pressure increased during the interval 0152 to ~0205 UT, and then was more-or-less constant thereafter. The ram pressure was generally decreasing during the outer magnetosphere passage (0226 to 0240 UT).

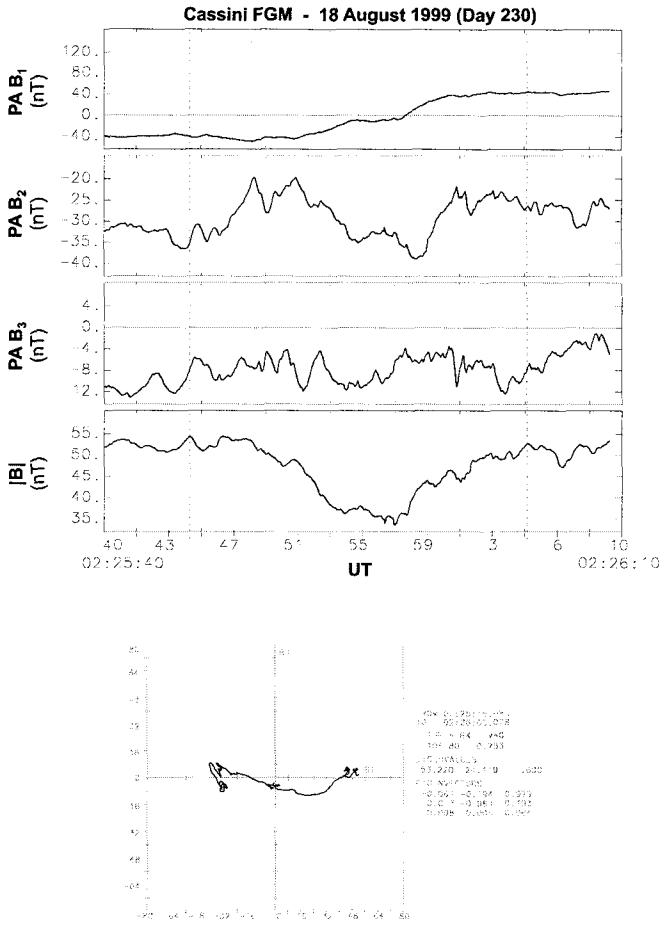

Fig. 5. The magnetic fields at the magnetopause (top panel). The bottom panel is a hodogram of the magnetopause fields.

The GEOTAIL interplanetary magnetic fields are given in Figure 6. The components were highly fluctuating, while the field magnitude remained relatively constant. The field component often changed abruptly. Previous studies by Ulysses investigations (Tsurutani et al., 1994; Smith et al., 1996) have shown that such magnetic fluctuations are another characteristic of high-speed streams. The fluctuations are outwardly propagating Alfvén waves. The abrupt component directional changes (rotational discontinuities) are the phase-steepened edges of the nonlinear Alfvén waves. The interplanetary Alfvén waves have been noted to be arc-polarized and spherical in nature (Tsurutani and Ho, 1999).

The shaded region indicates the time interval when Cassini was in the Earth's foreshock, magnetosheath and at the magnetopause. The interval is characterized by a large negative B_z component. This is noted to be a portion of an interplanetary Alfvén wave.

Foreshock Waves

Figure 7 is an overview plot of the foreshock waves, shown in high resolution. The wave amplitudes were largest near the shock, ~14 nT peak-to-peak in a ~35 nT field with decreasing amplitudes with increasing upstream distance. The waves had ~7.0 nT peak-to-peak amplitudes in an ~8 nT field at 0151:00 UT. The quasiperiod of the waves was ~0.8 s. The waves extended to unusually large distances from the shock, given that the interplanetary magnetic field was at such a large angle to the Sun-Earth line (~70°). Waves were clearly detected at 0150:00 UT, whereas the shock was at 0151:40 UT, giving a foreshock extent of ~5.6 x 10^4 km or ~8.5 R_e.

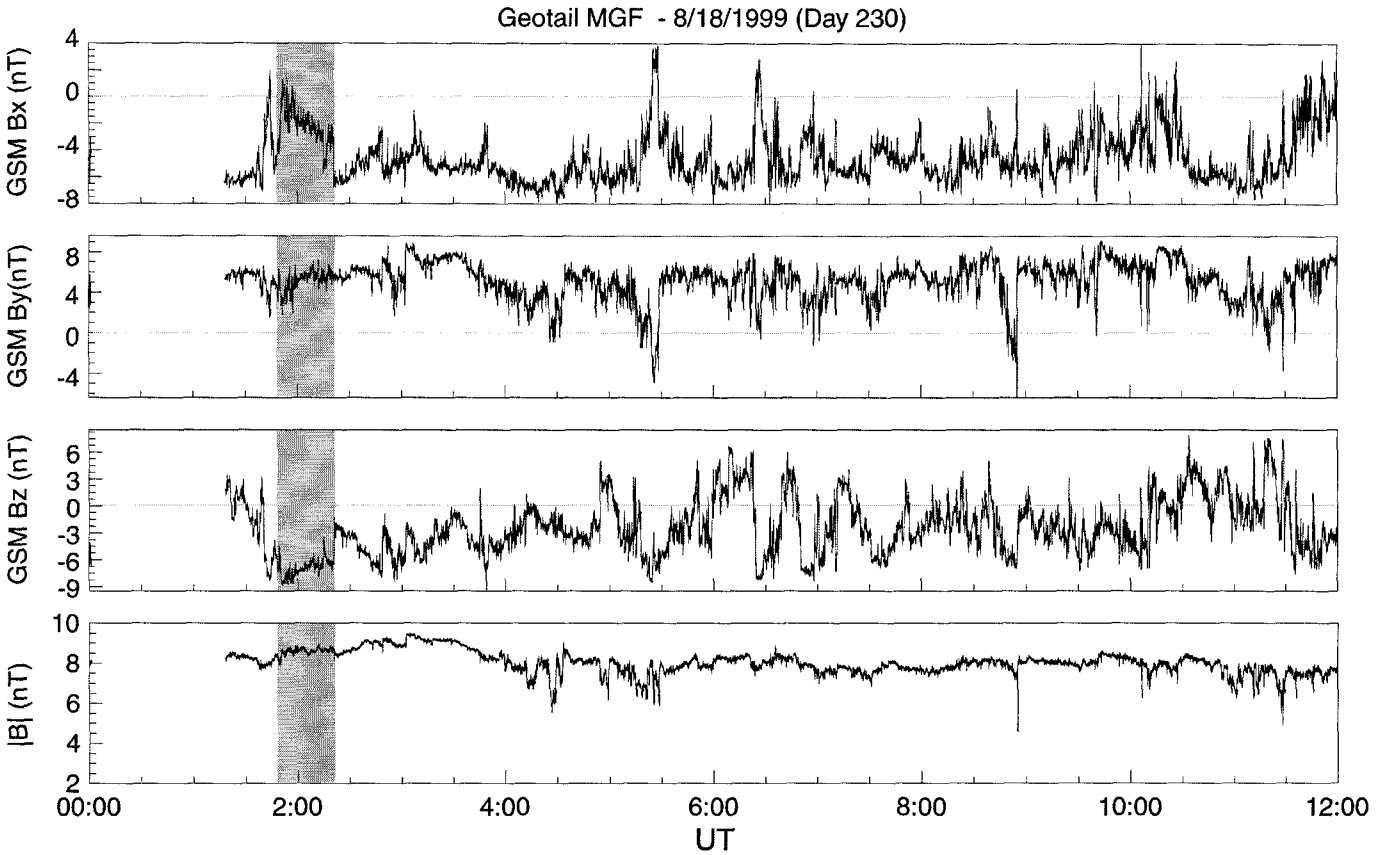

Fig. 6. The interplanetary magnetic field during the time of the Cassini Earth-encounter.

Figure 8 is an example of one wave cycle from 0151:39.9 to 0151:40.6 UT. The wave peak-to-peak amplitude is ~14.0 nT in a ~15 nT ambient field. In the hodogram it is noted that the wave was right-hand polarized in the spacecraft frame, nearly circularly polarized ($\lambda_1/\lambda_2 = 2.0$) and planar ($\lambda_2/\lambda_3 = 2.2$). Here the subscripts 1, 2 and 3 correspond to the maximum, intermediate and minimum variance components (Smith and Tsurutani, 1976). The angle of propagation relative to the ambient magnetic field θ_{kB} was ~52°.

Figure 9 is a wave cycle far from the shock, from 0151:16.6 to 0151:17.4 UT. The wave peak-to-peak amplitude was ~8.0 nT in a ~10.0 nT ambient field. The wave was right-hand circularly polarized ($\lambda_1/\lambda_2 = 1.9$), planar ($\lambda_2/\lambda_3 = 7.5$) and was propagating at an angle of 8° relative to the magnetic field. There was a ~2 nT compressional component associated with the wave.

Table 1 gives the wave properties for the entire foreshock interval. The waves were almost all right-hand circularly to elliptically polarized in the spacecraft frame. There were only a few left-hand wave cycles identified. The wave periods range between 0.3 s and 1.3 s in the spacecraft frame, with a median of 0.8 s. 45% of the waves had λ_1/λ_2 values between 1.0 and 3.0, indicating that the waves were often circularly to elliptically polarized. A normalized (to spherical area) histogram of θ_{kB} is given in Figure 10. The waves were propagating at all angles with respect to $\vec{B}$, with a slight tendency to propagate along the field line direction.

Calculation of Resonant Particle Energies (Generating the Foreshock Waves)

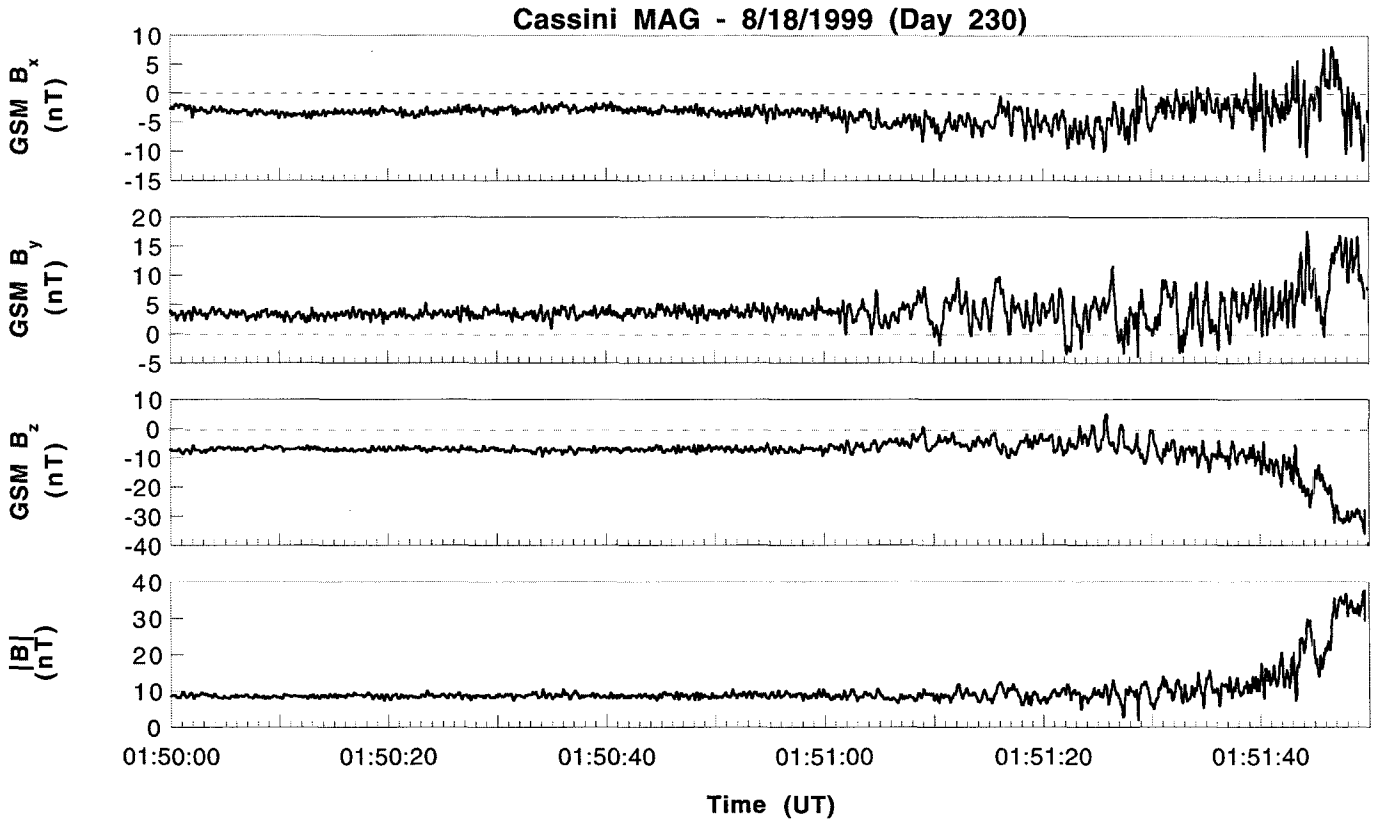

Fig. 7. The Earth's foreshock waves.

Foreshock plasma waves are generated by energetic protons or electrons that are streaming away from the bowshock/magnetosheath into the upstream region. In this particular case, the solar wind speed was ~560 km s^{-1} and the Alfvén speed ~10^7 km s^{-1}. The relevant ion, electron and plasma frequencies were 1.5 x 10^{-1} Hz, 2.3 x 10^2 Hz and 1.5 x 10^4 Hz.

Several features of the foreshock waves were unusual. First, the vast majority of the waves were right-hand polarized in the spacecraft frame. The waves had magnetic magnitude variations of ~25%, strong compressional components. Frequencies in the spacecraft frame were ~1.25 Hz (~0.8 s periods), considerably higher than ~10^{-1} to 1.3 x 10^{-2} unusually dominating foreshock waves (Hoppe et al., 1982). Also, the foreshock waves are typically left-hand polarized (in the spacecraft frame) rather than right-hand polarized as shown here. An additional interesting feature is the large angle between the interplanetary magnetic field and the solar wind velocity vector (~70°). The foreshock region remains quite large (~8.8 R_e in the x-direction), even with such a large field directional angle.

First order cyclotron resonance between waves and particles is given by:

$$f - \vec{k} \cdot \vec{V} = f_{\pm} \tag{1}$$

where f is the wave frequency, $\vec{k}$ the wave k vector, $\vec{V}$ the particle velocity vector and $f_{\pm}$ the particle ion or electron cyclotron frequency. Right-hand polarized waves detected in the spacecraft frame can be either left-hand waves propagating in the upstream direction but anomalously Doppler shifted by the solar wind to appear right-handed in the spacecraft frame, or they could be right-hand waves in the plasma frame propagating in the solar wind direction. For the latter case, the waves would be Doppler shifted to

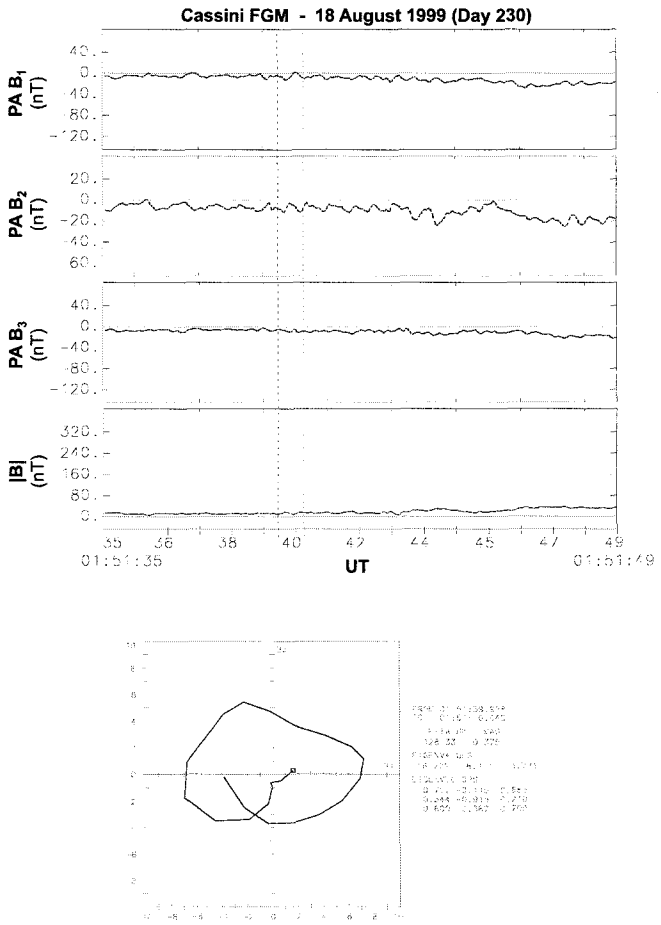

Fig. 8. Hodogram of the wave cycle from 01:51:39.9 to 01:51:40.6 UT.

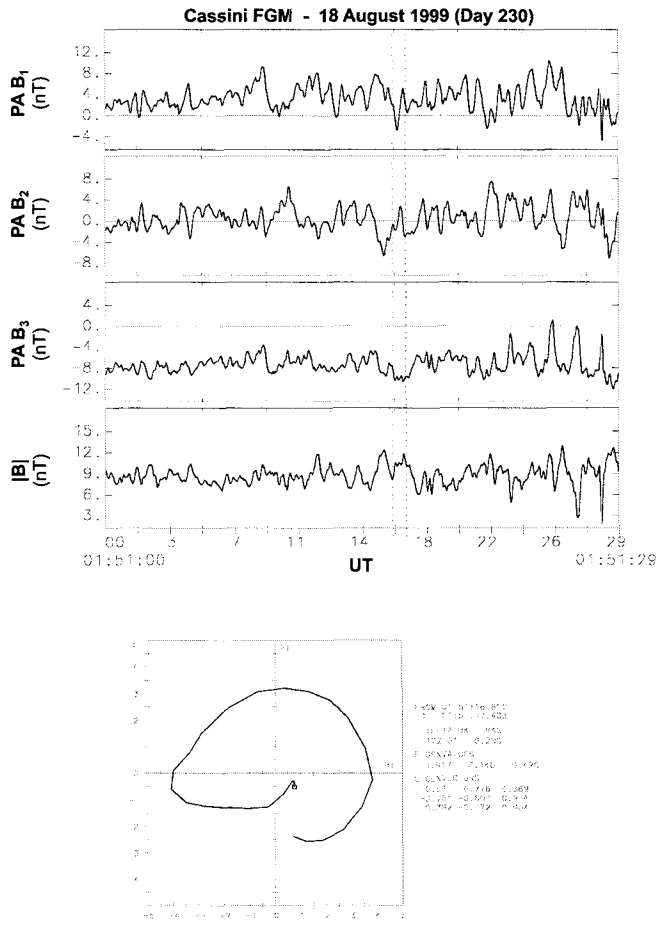

Fig. 9. Hodogram of the wave cycle from 01:51:16.6 to 01:51:17.4 UT.

higher frequencies. More detailed discussions of these various possibilities can be found in Tsurutani et al. (1983) and Tsurutani and Lakhina (1997).

Particles to be considered are therefore 1) sunward streaming protons and other ions which generate left-hand waves propagating in the solar direction, or 2) sunward streaming electrons generating right-hand waves propagating towards the Earth. The first possibility can be ruled out, as the resonant ion parallel speeds are too low for the particles to get upstream of the bow shock (not shown in detail to save space). There is the possibility that neutral atoms/molecules could be ionized in the upstream medium and this would lead to the generation of left-hand waves propagating towards the Sun (Barbosa and Eviatar, 1986; Goldstein et al., 1986). However, one might argue that sufficient neutral particle densities well upstream of the Earth seems an unlikely hypothesis and this possibility should be discounted. We therefore focus on the electron generation of magnetosonic (right-hand) waves hypothesis.

The cold plasma dispersion relation for parallel propagating right-hand waves is given by Stix (1962):

$$k^2c^2/\left(2\pi^2\right)f^2 = \left(f^2 - ff_e - f_ef_p - f_{pe}^2\right)\left(f + f_p\right)\left(f - f_e\right) \qquad (2)$$

Here f_e, f_p and f_{pe} are the electron, proton and plasma frequencies.

Since $f \sim f_p << f_e << f_{pe}$, the above expression can be simplified to:

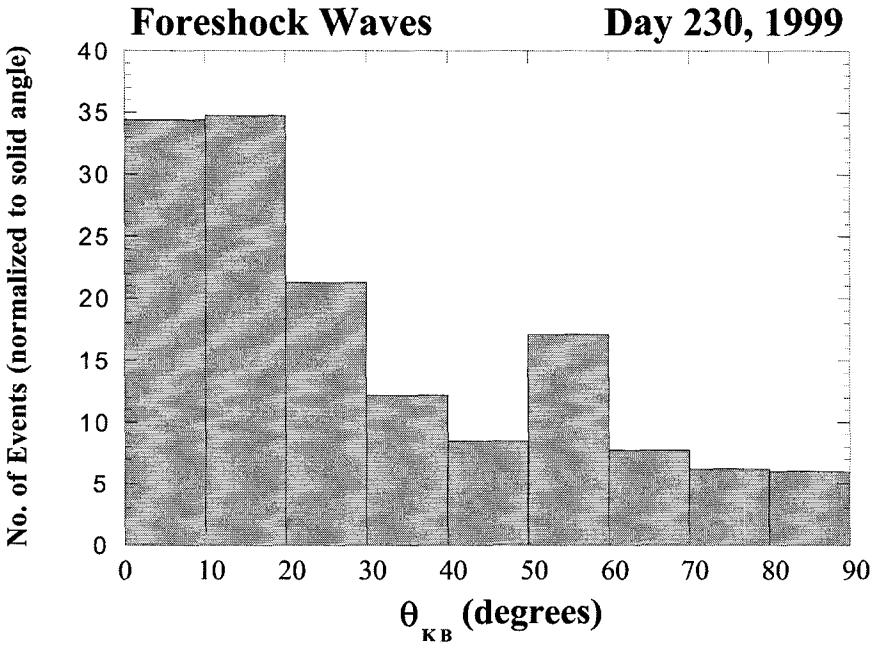

Fig. 10. A normalized histogram of the foreshock wave propagation directions.

$$V_{ph}^{\ 2} \approx V_A^{\ 2}\left(1 + f/f_p\right) \tag{3}$$

where V_{ph} is the wave phase speed and V_A the Alfvén wave speed (see Tsurutani et al., 1983). Assuming Earthward propagating right-hand waves, the Doppler shift relationship is:

$$f_{sc} = f_{sw}\left(V_{ph} + V_{sw}\cos\theta_{kV_{sw}}/V_{ph}\right) \tag{4}$$

In the above expression f_{sc} and f_{sw} are the wave frequencies in the spacecraft and solar wind reference frames. $\theta_{kV_{sw}}$ is the angle between the wave k vector and the solar wind velocity vector.

Using expressions (3) and (4), one gets V_{ph} ~2.6×10^7 cm s^{-1}, and from expression (1), $V_{\|} = 4.8 \times 10^9$cm s^{-1} or $E_{\|} = 6.5$ keV. Notice that the parallel electron velocity is more than adequate for the electrons to get into the upstream region.

Magnetosheath Waves

A sample of the magnetosheath waves is shown in Figure 11. The waves have 5-6 s quasisinusoidal periods with peak-to-peak amplitudes of ~8-10 nT in a ~34 nT field. The waves are thus highly nonlinear. There are large field magnitude decreases associated with some of the waves. The decreases involve field directional changes, thus they do not appear to be parts of mirror mode structures. It should be noted, however, that there is not a one-to-one association between waves and field decreases. There are more wave cycles than field decreases.

Figure 12 shows the wave-magnetic field decrease relationship in greater detail. Between the dashed vertical lines are 4 cycles of the waves. The magnetic field magnitude displays variations during two of the largest amplitude wave cycles (0157:07 - :12 and 0157:12 - :17 UT).

We will use two slightly different methods to determine the properties of the electromagnetic waves. We

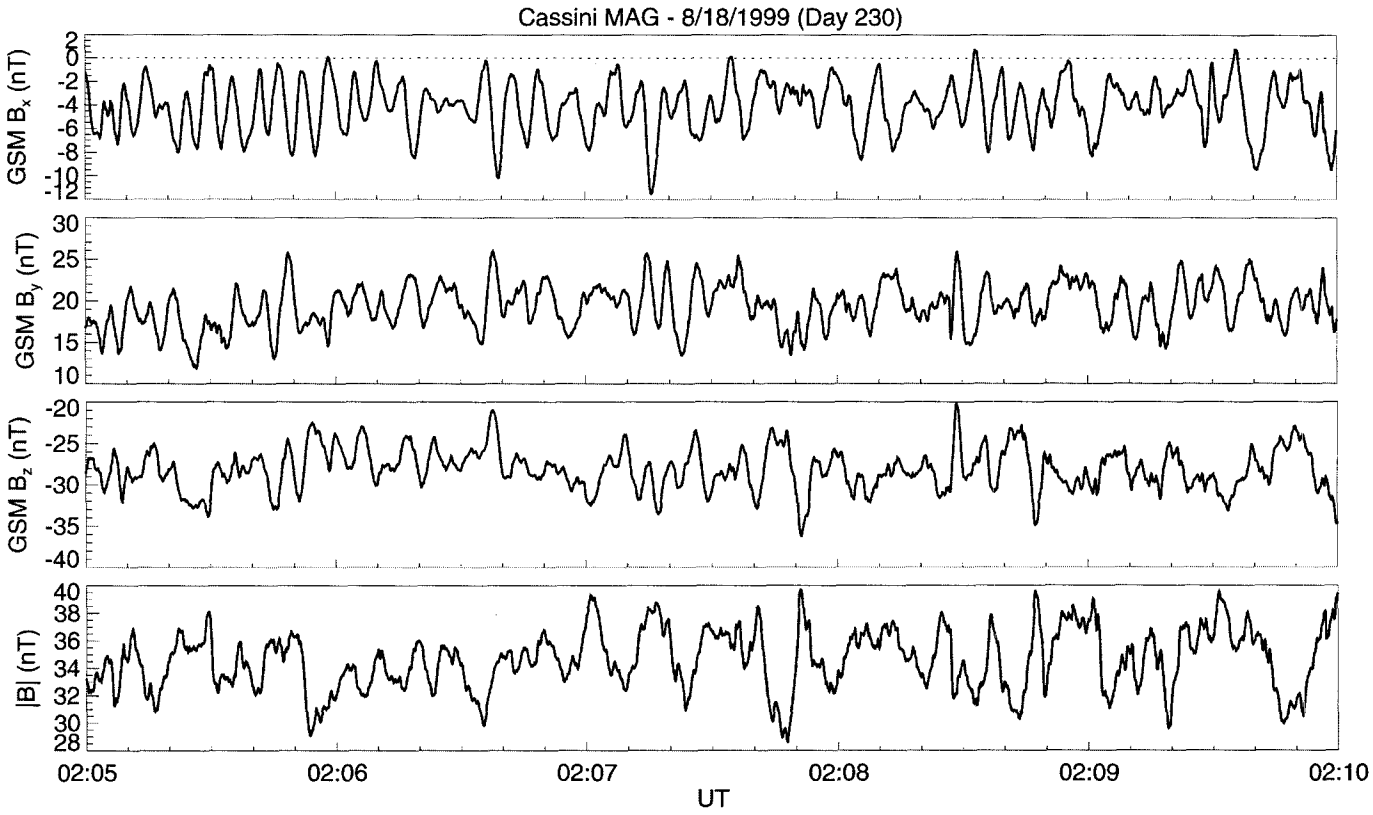

Fig. 11. Magnetosheath waves with 5 to 6 second quasiperiods and ~8-10 nT peak-to-peak amplitudes.

will use a minimum variance technique applied to single wave cycles and also applied to several wave cycles ("packets" - a packet is loosely defined as a number of cycles that appear to be roughly coherent) to compare and contrast the differences in the results. In some regions of space, wave properties vary from cycle to cycle, and thus multiple-cycle analyses could lead to a misunderstanding of the wave properties.

In Figure 13 we show the minimum variance analysis results for two consecutive wave cycles analyzed separately and also analyzed together (bottom panel). On the top is the cycle from 0157:03 - :08 UT and in the center, the cycle from 0157:08 - :15 UT. The wave cycle in the center is nearly circularly polarized in a left-hand sense, and is propagating at an angle of 6° relative to the ambient field. The wave is planar, $\lambda_2/\lambda_3 = 14.2$. The wave cycle in the center shows similar, but slightly different properties. The wave is planar ($\lambda_2/\lambda_3 = 11.2$) and is polarized in the left-hand sense. The wave is propagating at 18° relative to the ambient magnetic field and is elliptically polarized ($\lambda_1/\lambda_2 = 3.8$). The bottom panel shows the minimum variance results from the entire interval. Several differences can be noted: the multiple cycle "average" value indicates that the waves are far less planar ($\lambda_2/\lambda_3 = 3.7$), they are more circularly polarized ($\lambda_1/\lambda_2 = 1.8$), and the average propagation direction is nearly along $\vec{B}_O$ ($\theta_{kB} = 12.7°$).

Wave "packets" and individual cycles throughout the magnetosheath passage have been analyzed. A summary of the results is given in Table 2. The third and fourth columns are the start and stop times of the wave interval analyzed, the fifth column the average period of the waves in the packets ("packets" are denoted by the roman numerals in the first column), and B is the average ambient field strength in units of nT. Almost all cycles examined were found to be left-hand polarized in the spacecraft frame (right-hand column).

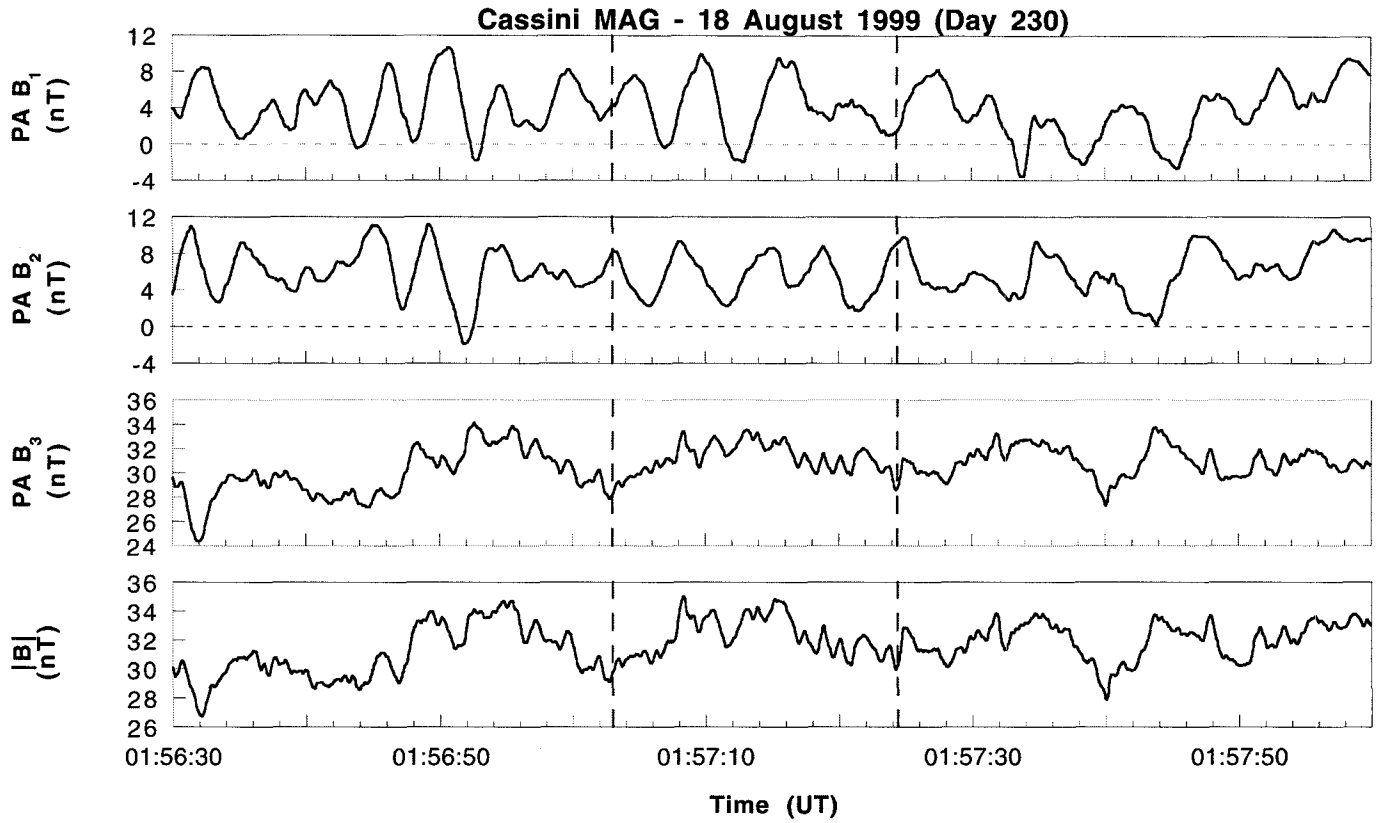

Fig. 12. Magnetosheath waves.

There are several interesting wave features to note in this table. The waves vary from circular to elliptical polarizations and the angles of propagation relative to the ambient magnetic field vary from 1° to 73°. Most of the waves are propagating obliquely to the ambient magnetic field. There is a general tendency, although not a strong one, for the obliquely propagating waves to be more elliptically polarized. However, there are examples of circularly polarized waves found to be propagating at very large θ_{kB} angles. An example can be found at 0205:48.6 to 05:55 UT ($\lambda_1/\lambda_2 = 1.8$ and $\theta_{kB} = 78°$).

The properties of the entire "packets" are shown in gray tone. The level of polarization (λ_1/λ_2) is typically near the minimum value of the individual cycle values within the packet. The angle of propagation θ_{kB} is also near the minimum of values of the individual cycles. Individual wave cycles within a "packet" often have similar angles of propagation (but not always). On the other hand, the degree of polarization of cycles within a packet is typically highly mixed.

Figure 14 gives the magnetosheath wave frequency (f) and the proton cyclotron frequency (f) as a function of spacecraft location (and time). Magnetospheric waves are also included in this plot (T > 0232 UT) but will not be discussed for the moment. The magnetosheath waves are noted to have frequencies of ~0.3 to 0.6 f_p.

Since the magnetosheath fields were essentially orthogonal to the Sun-earth line, the Doppler shift of the waves due to convection past the spacecraft was negligible. Thus the waves are left-hand polarized in the plasma frame and were propagating in the proton (ion) cyclotron mode. We believe that these are the largest amplitude proton cyclotron waves detected in geospace to date.

From an inspection of the magnetic field data, it was found that there was little or no indication of the presence of mirror mode structures. A search for field decreases with little or no changes in direction

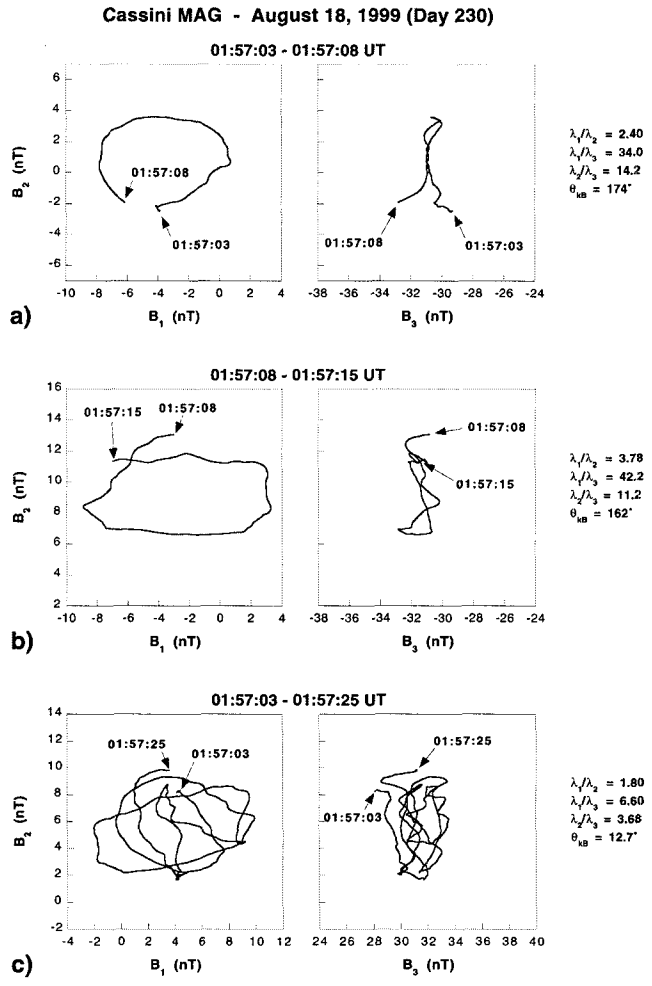

Fig. 13. Several magnetosheath wave cycles. The events were taken from the interval in Figure 12.

proved to be unfruitful. Few, if any, intense whistler lion roars (often associated with the high beta portions of mirror mode structures: Tsurutani et al., 1982; Zhang et al., 1998; Paschmann et al., 2000) were detected in the magnetosheath (G. Hospodarsky, personal communication, 2000).

Outer Magnetospheric Waves

An example of the outer magnetospheric waves is shown in Figure 15. The waves are quasi-sinusoidal with ~3 s periods. The maximum peak-to-peak amplitudes are ~3.0 nT in a ~61 nT field (at ~0232:30 UT). The wave amplitudes are largest in the transverse components (GSM B_y and B_x). The ambient field is primarily in B_z, as expected for magnetospheric fields. The amplitude is largest in the B_y component and is considerably smaller in the B_x component. The waves sometimes have a compressional component. At ~0232:30 UT, the magnetic magnitude (compressional) variations are on the order of ~0.5 nT.

Figure 16 shows the waves in minimum variance coordinates and in higher time resolution. It is interesting to note that the amplitudes are largest (8.5 nT peak-to-peak) where the magnetic field increased from ~61 to ~62 nT. The interval between 0232:30 and 0232:46 UT has been used to determine the minimum variance coordinates for the whole interval of the figure. The B_3 component oscillations are minimum in this region, indicating an accurate determination of the minimum variance direction. On the bottom (panel b) are the corresponding hodograms. The B_2 - B_1 hodogram indicates that the waves are

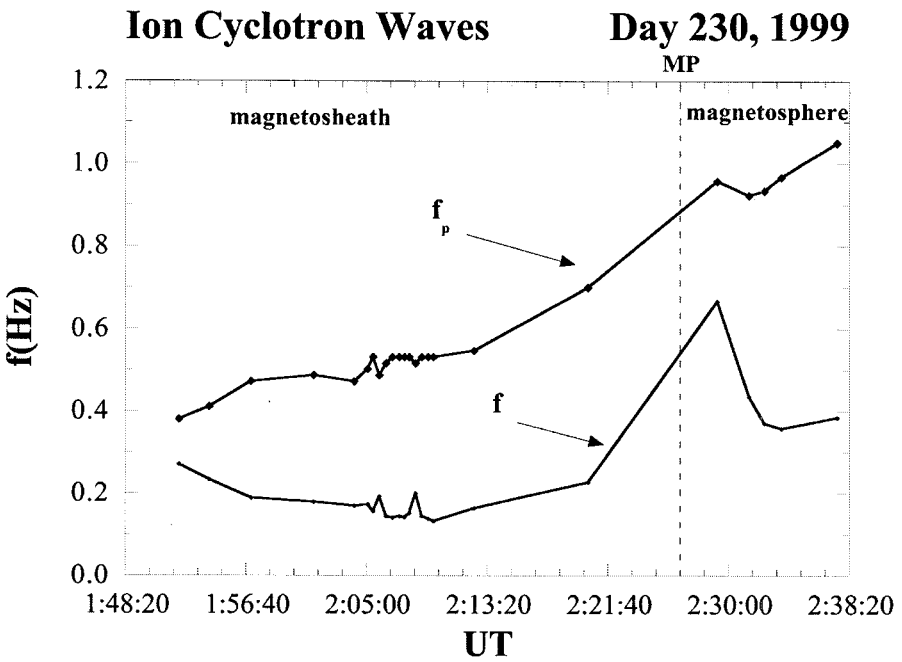

Fig. 14. Magnetosheath and magnetospheric wave frequency as a function of proton cyclotron frequency.

highly linearly polarized (consistent with the previous description of B_y and B_x amplitudes). The individual wave cycles are shifted from each other in the hodogram because of the spacecraft motion toward the Earth into higher magnetic field strengths (we specifically did not detrend the data). The B_2 - B_3 hodogram shows that the waves are reasonably planar. The angle of propagation of the waves relative to the magnetic field was ~42°.

Individual cycles of the magnetosheath waves have been analyzed and the results are given in Table 2. The range of polarization λ_1/λ_2 is 1.4 to 27.5 and the range of angle θ_{kB} was 1° to 73°.

Figure 17 shows another example of the outer magnetospheric waves, but later in time. The amplitudes are as large as ~2.0 nT peak-to-peak in a ~69.0 nT ambient field. There is a slight magnetic field magnitude gradient where the waves were detected. The interval where the minimum variance analyses were performed is indicated by the two vertical dashed lines at 0237:24 UT and 0237:41 UT. Again there is very little variation along B_3, indicating a "good determination" of the minimum variance direction. The magnetic magnitude variations associated with the waves are quite small, ~0.2 nT (note that the scale of the B_3 component and $|B|$ is much finer than for the other components).

The bottom panel (b) gives the hodogram results. These waves are left-hand elliptically polarized with λ_1/λ_2 = 2.9. The average angle of propagation is 8.6° relative to $\vec{B}$. The waves are highly plane polarized, $\lambda_1/\lambda_3 = 212$ and $\lambda_2/\lambda_3 = 73.1$.

The magnetospheric wave results are itemized in Table 3. All of the waves analyzed were found to be left-hand circularly to linearly polarized (λ_1/λ_2 up to 175) in the spacecraft frame. The θ_{kB} values range from 6° to 71°. Some packets have nearly parallel propagating waves and other packets are off-axis propagating waves. Since there is little or no plasma convection to speak of, the waves must be left-hand polarized in the plasma frame. From Figure 14, the waves have a frequency f between 0.3 and 0.5 f_p. The waves are therefore propagating in the proton cyclotron mode.

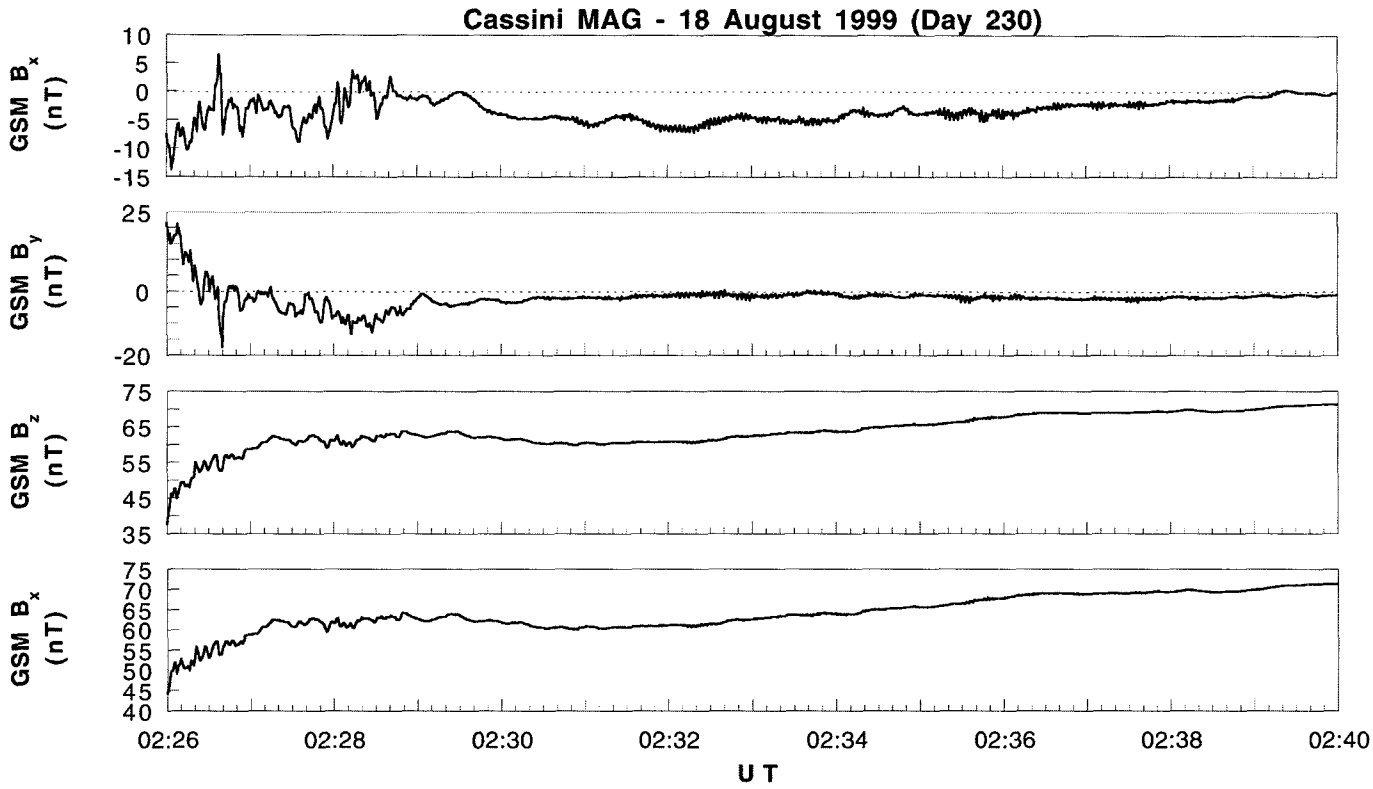

Fig. 15. Outer magnetospheric waves.

To determine the solar wind effects on the magnetosphere during this interval, we again examine the GEOTAIL ram pressure values/variations given in Figure 3. The interval of outer magnetospheric waves occurs from 0226 UT to 0238 UT (Figures 15 to 17). As previously stated, the time delay for the solar wind to travel from GEOTAIL to the magnetopause is ~4 min. Thus, the relevant solar wind plasma parcel is from ~0222 to 0234 UT.

Can one find solar wind features that lead to proton temperature anisotropies $(T_\perp / T_\parallel > 1)$ that cause ion cyclotron wave growth? There are no obvious large scale solar wind ram pressure fluctuations that caused the growth of the waves such as were found by Anderson and Hamilton (1993) in their events. However, the relationship between large amplitude waves and magnetic field increases noted in Figures 16 and 17 indicates that small ram pressure fluctuations may be present. If so, there could be small scale density enhancements that would easily be missed by GEOTAIL. Perhaps future Cluster II searches for small solar wind features and their effects will answer this question.

Particle Losses and Proton Auroras

The peak proton cyclotron wave amplitudes of ±1.7 nT in a 61 nT field occurred at ~0232 UT. The proton cyclotron frequency f_p was 0.93 Hz. The wave frequency f was ~0.35 Hz. Assuming a wave phase velocity $V_{ph} \approx 10^8$ cm^{-2} s^{-1}, and using the first-order cyclotron resonance condition (1), one obtains a resonant proton parallel energy of ~10 keV. The pitch angle diffusion rate is given by:

$$D_{\alpha\alpha} = 2\pi f_p \left(\frac{B_\omega}{B}\right)^2 \eta \qquad (5)$$

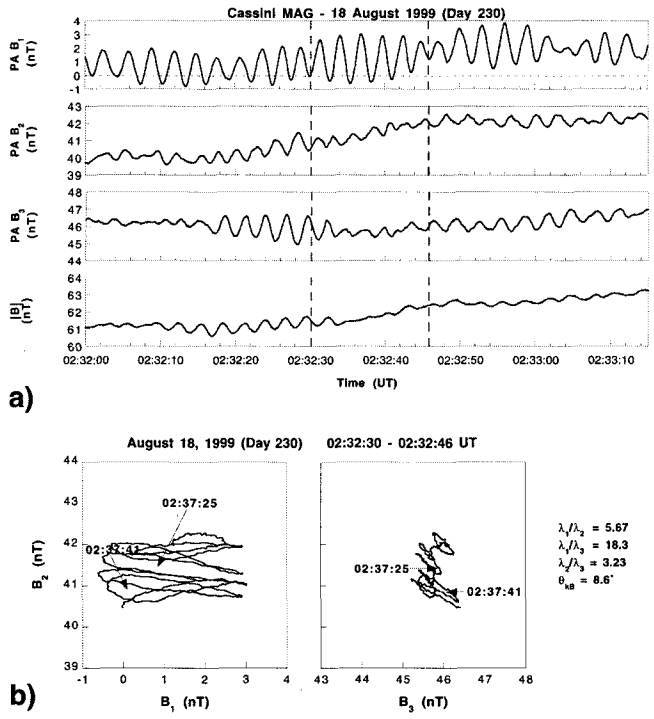

Fig. 16. Hodogram of the 02:32:30 to 02:32:46 UT magnetospheric wave packet.

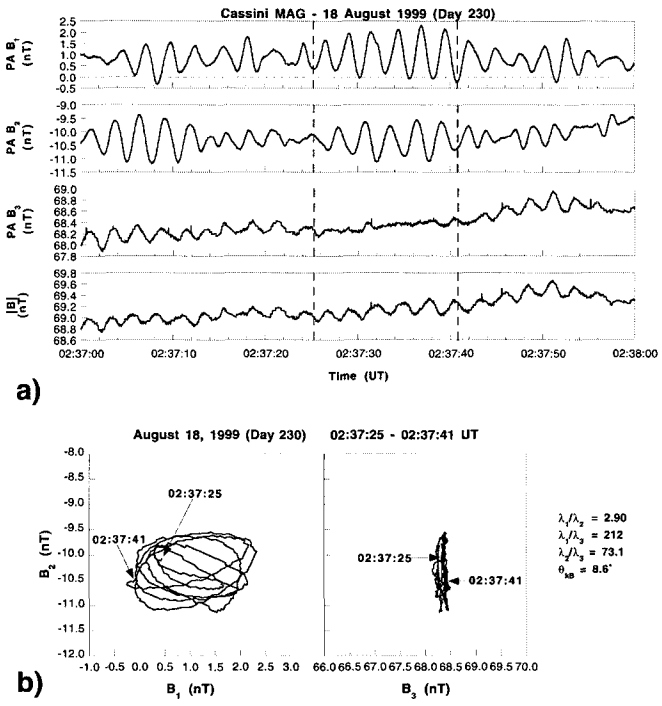

Fig. 17. A hodogram of the 02:37:24 to 02:37:41 UT wave packet.

from Kennel and Petschek (1966). With a value of $B_\omega \approx 1.7$ nT, and assuming η the fractional amount of time the particle is in resonance with the wave is ≈ 0.1, $D_{\alpha\alpha}$ is therefore ~7.2×10^5 s^{-1}, or $T = 1.3 \times 10^4$ s. The bounce time T_b of a 10 keV proton is 1.2×10^2 s. Thus the protons are on weak pitch angle diffusion. The resulting proton aurora due to wave-particle interactions would be expected to be weak and diffuse.

Magnetotail Waves

The Alfvénic B_s fluctuations (shown in Figure 6) caused magnetospheric substorms. Corresponding geomagnetic activity was high throughout the Cassini pass. This is shown in Figure 18. Substorms were occurring from ~0700 to ~1200 UT, the Cassini tail passage. Large amplitude waves in the tail lobe were detected primarily near two time regions, ~0810 and 1010 UT. This is indicated in the figure.

One example of waves near the former interval is shown in Figure 19. The waves are transverse oscillations, and have ~7.5 s periods. The peak-to-peak amplitudes are ~0.3 nT in a ~16.1 nT field. The compressional components are ≤ 0.1 nT. The three cycles from 0819:43.7 to 0820:07.6 UT are elliptically polarized $\left(\lambda_1 / \lambda_2 = 2.3 \text{ to } 3.0 \right)$ and are propagating nearly along $\vec{B}$ (6° to 26°).

Figure 20 shows an example of the waves detected in the second interval. Nearly purely compressional (longitudinal) oscillations with ~7.3 s periods are present. The magnitude is again small, ~0.1 nT. The four cycles from 1003:15.6 to 1003:44.4 UT are compressive waves. The angles of propagation are highly oblique to $\vec{B}$ (76°, 84°, 70° and 75°). We believe that this is the first time such purely compressional waves have been detected in the magnetotail.

The extremely thorough Cassini magnetic control program instituted by the Project has developed this very low-noise spacecraft (Mehlem and Narvaez, 1999). Without such a rigorous program it is probable that such new wave modes could not have been detected.

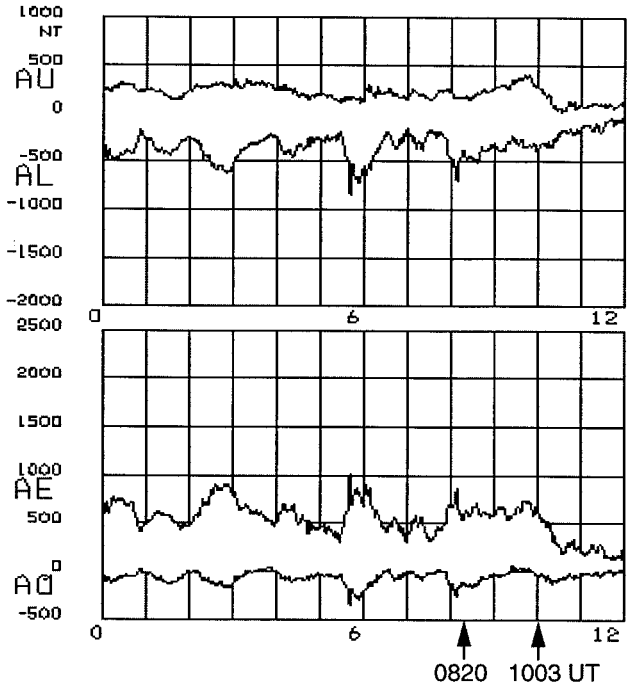

Fig. 18. Auroral zone geomagnetic indices during the Cassini flyby. Two intervals where LF waves were detected are indicated by arrows.

SUMMARY

Foreshock Waves

Foreshock waves are detected in the region from the shock to ~8.8 R_e upstream. The waves have ~0.8 s quasiperiods in the plasma frame and are right-hand circularly to elliptically polarized in the spacecraft frame. The angle of propagation to $\vec{B}$ varies from 6° to 88°. The waves are compressive. It is argued that the foreshock is a pure electron foreshock and the waves are magnetosonic mode emissions generated by ~6.5 keV electrons streaming towards the Sun. This is considerably different than typical foreshocks where the angle between the interplanetary magnetic field and the solar wind velocity is ~45°. For large $\theta_{BV_{sw}}$ angles, as in the case presented here, only energetic electrons will have the necessary velocity to get upstream to form a foreshock (Tsurutani and Rodriguez, 1981).

Magnetosheath Waves

The magnetosheath waves are found to be left-hand circular to elliptically polarized with $f = 0.3$ to $0.6\ f_p$. They are generated by a temperature anisotropy instability with $T_\perp/T_\parallel > 1$. The anisotropy is created by the shock heating of solar wind protons, in direction perpendicular to the magnetic field, at the shock. Behind the shock and throughout the sheath, the Zwan-Wolf (1976) draping effect will maintain a strong $T_\perp/T_\parallel > 1$ anisotropy. The magnetosheath proton cyclotron waves are the most intense ion cyclotron waves detected in geospace to date.

Magnetospheric Waves

The outer magnetosphere waves are also identified as proton cyclotron waves with frequencies between 0.2 to 0.5 f_p. These waves are often highly elliptical to linearly polarized. The source of free energy is,

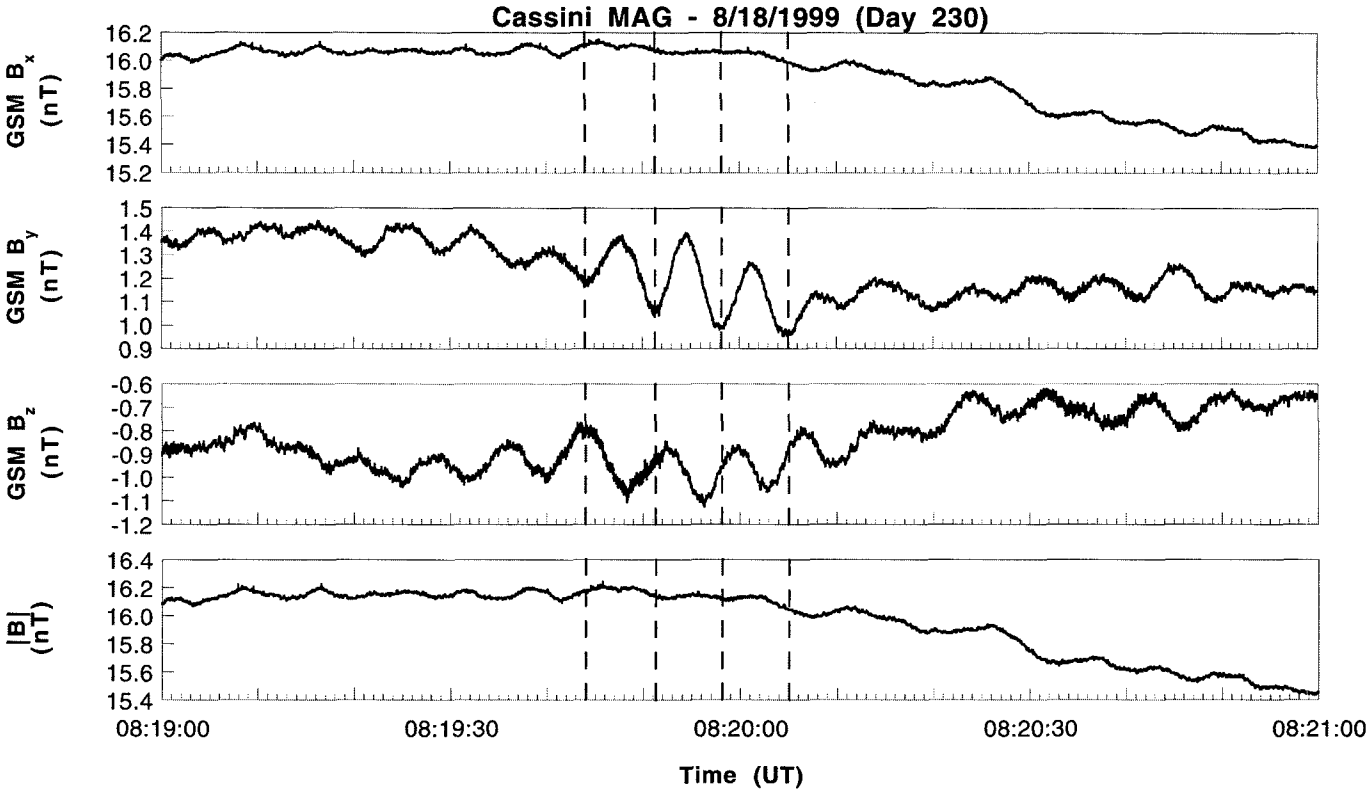

Fig. 19. Transverse ~7.5 second oscillations in the magnetotail.

however, somewhat of a mystery. At the time of wave occurrence, the large scale solar wind ram pressure was steady to decreasing. Small scale solar wind fluctuations cannot be ruled out, however.

Magnetotail Waves

Two new modes were identified in the distant tail lobes, primarily due to the unusual sensitivity of the Cassini magnetometers and the spacecraft cleanliness program. A purely compressive (~0.1 nT) mode as well as a short period transverse wave mode were illustrated.

CONCLUSIONS AND DISCUSSION

In the Cassini geospace wave survey, we find that much can be done to understand microinstabilities generating LF waves using magnetic field data alone. From our results, we have been able to make a variety of predictions of plasma and energetic particle pitch angle distributions (in the foreshock, magnetosheath and outer magnetosphere). In a follow-up effort, we will examine the plasma and energetic particle and wave properties to determine if our conclusions/speculations in this paper were indeed correct or not.

This paper has shown that even though these four regions of space have been previously studied in very great detail, there is still much to learn and it is very worthwhile examining the waves in even greater detail. Cluster II will provide an opportunity for detailed studies of several of these regions.

Many surprises were found from this examination. In the foreshock, the standard picture is that ion beams stream from the shock/magnetosphere into the upstream region. These beams generate foreshock waves. The mode typically reported in the literature (Hoppe, 1981; Smith et al., 1983; Tsurutani et al.,

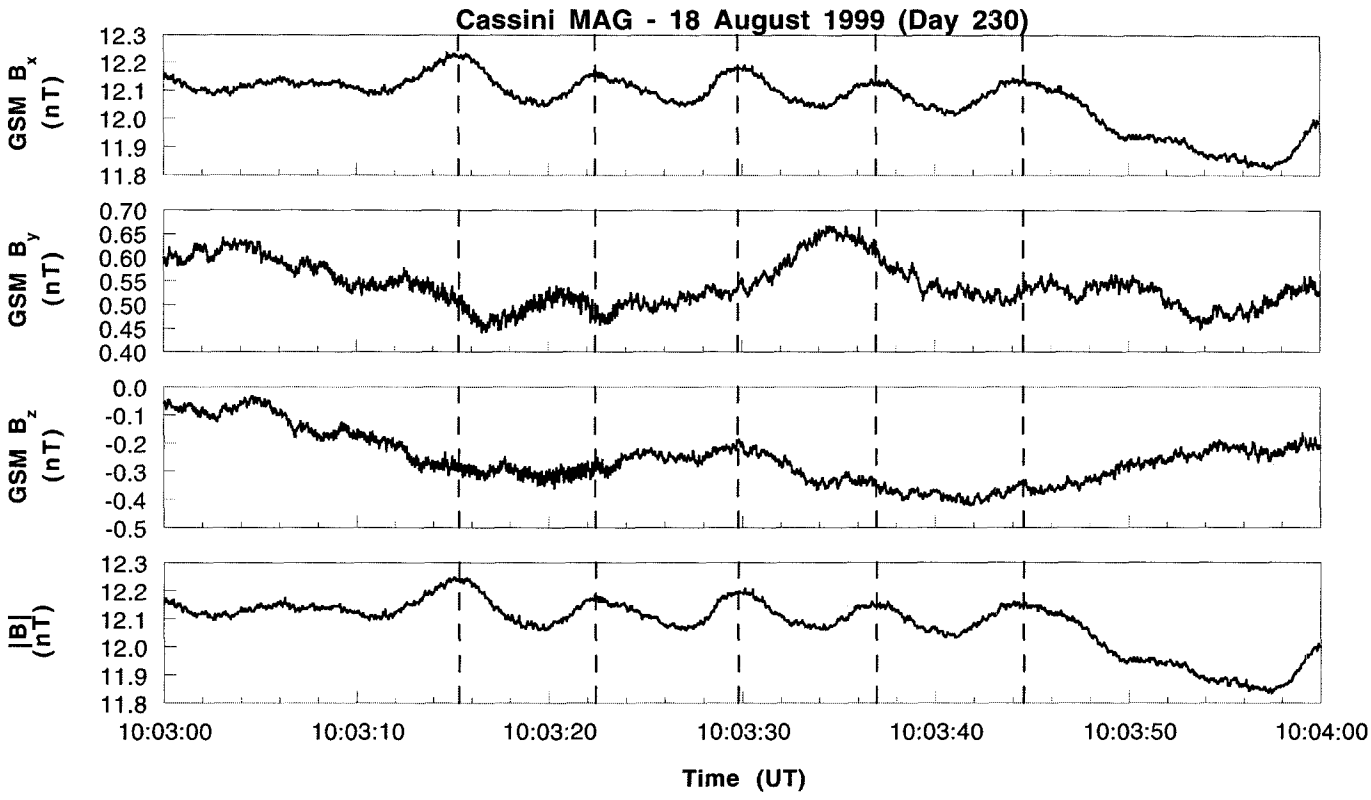

Fig. 20. Nearly purely compressional ~7.3 s waves in the magnetotail.

1993) has 10 - 60 s periods is and left-hand polarized in the spacecraft frame. These waves have been shown to be anomalously Doppler shifted magnetosonic (right-hand) waves convected past the spacecraft. However, here we show a purely electron foreshock filled with high frequency 1.25 Hz whistler mode (magnetosonic) waves. The dominance of electrons forming the foreshock is due to the very large angle that the magnetic fields make with respect to the Earth-Sun line.

The magnetosheath waves are perhaps the biggest surprise. No mirror mode structures were detected. Only proton cyclotron waves were present and these had the largest amplitude (of ion cyclotron waves) detected in geospace to date. The ACE He^{++}/H^{+} density ratio was ~ 2.0% for the solar wind plasma parcel that hit the bowshock at the time of the Cassini encounter. This low He^{++} density ratio is in qualitative agreement with the Price et al. (1986) and Gary et al. (1992) scenario of a reduction in size of the stop-band, thus an increase in the ion cyclotron growth rate. However, further modeling work needs to be done to understand if this is indeed the correct explanation or not. We further note that the He^{++}/H^{+} ratio varied from <1% (at the peak of the event) to 4% (at the edges of the event) within the high-speed stream. Whether this variability is a feature of high-speed streams detected in the ecliptic plane where stream "edge effects" and fast stream-slow stream interactions are important, needs to be studied. For these reasons, the variability of Jovian and Saturnian magnetosheath wave modes and intensities (also under the different plasma beta conditions) are of particular interest for future Cassini studies.

One possible scenario explaining the presence of dayside instabilities/waves is that the previously occurring substorms have led to proton injection in the midnight sector. With subsequent particle gradient and curvature drift to the dayside, the asymmetric shape of the magnetosphere (compressed dayside) leads to particle drift-shell splitting (Roederer, 1967; Schulz, 1972), where particles with ~90° pitch angle will drift to larger L than particles with near ~0° pitch. This picture will lead to "patches" in the outer dayside magnetosphere where the proton cyclotron mode would be unstable. A second scenario,

working in conjunction with the first, can lead to the enhanced wave growth. If sunlight heating of the ionosphere leads to upward flow of plasma and an enhanced magnetospheric cold population, the presence of this plasma would lead to a lowering of the resonant energy threshold for instability. A similar explanation has been proposed to explain enhanced chorus (electron temperature anisotropy instability) at local dawn (Jensch, 1976, Tsurutani and Smith, 1977) through the electron temperature anisotropy instability. A third factor discussed previously is the possible presence of small scale solar wind pressure pulses. At any rate, the proton cyclotron waves are clearly present and will lead to a steady "drizzle" of particles into the upper ionosphere. To determine the specific mechanisms, energetic particle pitch-angle information and plasma densities will have to be examined in detail. We hope to do this in the near future.

ACKNOWLEDGMENTS

Portions of the research presented here were performed at the Jet Propulsion Laboratory, California Institute of Technology, Pasadena, under contract with the National Aeronautics and Space Administration.

REFERENCES

Anderson, B. T., and D. C. Hamilton, Electromagnetic Ion Cyclotron Waves Stimulated by Modest Magnetospheric Compressions, *J. Geophys. Res.*, **98**, 11369 (1993).

Anderson, B. J., S. A. Fuselier, S. P. Gary, and R. E. Denton, Magnetic Spectral Signatures in the Earth's Magnetosheath and Plasma Depletion Layer, *J. Geophys. Res.*, **99**, 5877 (1994).

Armstrong, T. P., M. E. Pesses, and R. B. Decker, Shock Drift Acceleration, in *Collisionless Shocks in the Heliosphere: Reviews of Current Research*, ed. B. T. Tsurutani and R. G. Stone, Geophys. Mon., **35**, pp. 271-285, Amer. Geophys. Union Press, Wash. D.C. (1985).

Asbridge, J. R., S. J. Bame, and I. B. Strong, Outward Flow of Protons from the Earth's Bow Shock, *J. Geophys. Res.*, **73**, 5777 (1968).

Baker, D. N., R. D. Belian, T. A. Fritz, P. R. Higbie, S. M. Krimigis, D. G. Sibeck, and R. D. Zwickl, Simultaneous Energetic Particle Observations at Geostationary Orbit and in the Upstream Solar Wind: Evidence for Leakage During the Magnetospheric Compression Event of November 1, 1984, *J. Geophys. Res.*, **93**, 14317 (1988).

Barbosa, D. D., and A. Eviatar, Planetary Fast Neutral Emission and Effects on the Solar Wind: A Cometary Exosphere Analog, *Astrophys. J.*, **310**, 927 (1986).

Brinca, A. L., and B. T. Tsurutani, Influence of Multiple Ion Species on Low-Frequency Electromagnetic Wave Instabilities, *J. Geophys. Res.*, **94**, 13565 (1989).

Bonifazi, C., and G. Moreno, Reflected and Diffuse Ions Backstreaming from the Earth's Bow Shock, 1. Basic Properties, *J. Geophys. Res.*, **86**, 4397 (1981a).

Bonifazi, C., and G. Moreno, Reflected and Diffuse Ions Backstreaming from the Earth's Bow Shock, 2. Origin, *J. Geophys. Res.*, **86**, 4405 (1981b).

Cowley, S. W. H., R. J. Hynds, I. G. Richardson, P. W. Daly, T. R. Sanderson, K.-P. Wenzel, J. A. Slavin, and B. T. Tsurutani, Energetic Ion Regimes in the Deep Geomagnetic Tail: ISEE-3, *Geophys. Res. Lett.*, **11**, 275 (1984).

Dougherty, M. K., S. Kellock, D. J. Southwood, A. Balogh, M. Barlow, T. Beek, M. W. Dunlop, R. White, E. J. Smith, L. Wigglesworth, M. Fong, R. Marquedant, B. T. Tsurutani, B. Gerlach, G. Musmann, K.-H. Glassmeier, H. Hartje, M. Rahm, I. Richter, C. T. Russell, D. Huddleston, R. C. Snare, G. Erdos, S. Szalai, F. M. Neubauer, S. W. H. Cowley, and G. L. Siscoe, The Cassini Magnetic Field Investigation, *Space Sci. Rev.*, submitted (2000).

Dungey, J. W., Interplanetary Magnetic Field and the Auroral Zones, *Phys. Res. Lett.*, **6**, 47 (1961).

Fairfield, D. H., Bow Shock Associated Waves Observed in the Far Upstream Interplanetary Medium, *J. Geophys. Res.*, **74**, 3541 (1969).

Forman, M. A., and G. M. Webb, Acceleration of Energetic Particles, in *Collisionless Shocks in the Heliosphere: A Tutorial Review*, ed. R. G. Stone and B. T. Tsurutani, Geophys. Mon., **34**, pp. 91-114, Amer. Geophys. Union Press, Wash. D.C. (1985).

Gary, S. P., C. D. Madland, and B. T. Tsurutani, Electromagnetic Ion Beam Instabilities, II., *Phys. Fluids*, **28**, 3691 (1985).

Gary, S. P., Electromagnetic Ion/Ion Instabilities and their Consequences in Space Plasmas: A Review, *Space Sci. Rev.*, **56**, 373 (1991).

Gary, S. P., The Mirror and Ion Cyclotron Anisotropy Instability, *J. Geophys. Res.*, **97**, 8519 (1992).

Goldstein, M. L., H. K. Wong, A. F. Vinas, and C. W. Smith, Large Amplitude MHD Waves Up Stream of the Jovian Bow Shock: Reinterpretation, *J. Geophys. Res.*, **90**, 302 (1985).

Goldstein, M. L., H. K. Wong, and A. Eviatar, Excitation of MHD Waves Upstream of Jupiter by Energetic Sulfur on Oxygen Ions, *J. Geophys. Res.*, **91**, 7954 (1986).

Goodrich, C. C., Numerical Simulations of Quasi-Perpendicular Collisionless Shocks, in *Collisionless Shocks in the Heliosphere: Reviews of Current Research*, ed. B. T. Tsurutani and R. G. Stone, Geophys. Mon., **35**, pp. 153-168, Amer. Geophys. Union Press, Wash. D.C. (1985).

Hoppe, M. M., C. T. Russell, L. A. Frank, T. E. Eastman, and E. W. Greenstadt, Upstream Hydromagnetic Waves and their Association with Backstreaming Ion Populations: ISEE 1 and 2 Observations, *J. Geophys. Res.*, **86**, 4471 (1981).

Jensch, V., Electron Precipitation in the Morning Sector of the Auroral Zone, *J. Geophys. Res.*, **81**, 135 (1976).

Kennel, C. F., J. P. Edmiston, and T. Hada, A Quarter Century of Collisionless Shock Research, in *Collisionless Shocks in the Heliosphere: A Tutorial Review*, ed. R. G. Stone and B. T. Tsurutani, Geophys. Mon., **34**, pp. 1-36, Amer. Geophys. Union, Wash. D.C. (1985).

Lee, M. A., Coupled Hydromagnetic Wave Excitation and Ion Acceleration Upstream of the Earth's Bow Shock, *J. Geophys. Res.*, **87**, 5063 (1982).

McComas, D. J., G. W. Hoogeveen, J. T. Gosling, J. L. Phillips, M. Neugebauer, A. Balogh, and R. Forsyth, Ulysses Observations of Pressure-Balance Structures in the Polar Solar Wind, *Astron. Astrophys.*, **316**, 368 (1996).

Mehlem, K., and P. Narvaez, Magnetostatic Cleanliness of Radioisotopic Thermoelectric Generators (RTGs) of Cassini, IEEE, 899 (1999).

Papadopoulos, K., Microinstabilities and Anomalous Transport, in *Collisionless Shock in the Heliosphere: A Tutorial Review*, ed. R. G. Stone and B. T. Tsurutani, Geophys. Mon., **34**, pp. 59-90, Amer. Geophys. Union Press, Wash. D.C. (1985).

Petrinec, S. M., and C. T. Russell, Near-Earth Magnetotail Shape and Size as Determined from the Magnetopause Flaring Angle, *J. Geophys. Res.*, **101**, 137 (1996).

Phillips, J. L., A. Balogh, S. J. Bame, B. E. Goldstein, J. T. Gosling, J. T. Hoeksema, D. J. McComas, M. Neugebauer, N. R. Sheeley, Jr., and Y. M. Wang, Ulysses at 50° South: Constant Immersion in the High-Speed Solar Wind, *Geophys. Res. Lett.*, **21**, 1105 (1994).

Price, C. P., D. W. Swift, and L. C. Lee, Numerical Simulation of Nonoscillatory Mirror Waves at the Earth's Magnetosheath, *J. Geophys. Res.*, **91**, 101 (1986).

Roederer, J. G., On the Adiabatic Motion of Energetic Particles in a Model Magnetosphere, *J. Geophys. Res.*, **72**, 981 (1967).

Schulz, M., Drift-Shell Splitting at Arbitrary Pitch Angle, *J. Geophys. Res.*, **77**, 624 (1972).

Sibeck, D. G., R. W. McEntire, S. M. Krimigis, and D. N. Baker, The Magnetosphere as a Sufficient Source for Upstream Ions on November 1, 1984, *J. Geophys. Res.*, **93**, 14328 (1988).

Smith, E. J., and B. T. Tsurutani, Magnetosheath Lion Roars, *J. Geophys. Res.*, **81**, 2261 (1976).

Smith, E. J., B. T. Tsurutani, D. L. Chenette, T. F. Conlan, and J. A. Simpson, Jovian Electron Bursts, Correlation with the Interplanetary Field Direction and Hydromagnetic Waves, *J. Geophys. Res.*, **81**, 65 (1976).

Smith, C. W., M. L. Goldstein, and W. H. Mathaeus, Turbulence Analysis of the Jovian Upstream Wave Phenomena, *J. Geophys. Res.*, **88**, 5581 (1983).

Sonnerup, B. U. O., and B. G. Ledley, Magnetopause Rotational Forms, *J. Geophys. Res.*, **79**, 4309 (1974).

Thomsen, M. F., Upstream Suprathermal Ions, in *Collisionless Shocks in the Heliosphere: Reviews of Current Research*, ed. B. T. Tsurutani and R. G. Stone, Geophys. Mon., **35**, pp. 253-270, Amer. Geophys. Union Press, Wash D.C. (1985).

Tsurutani, B. T., and E. J. Smith, Two Types of Magnetospheric ELF Chorus and their Substorm Dependences, *J. Geophys,. Res.*, **82**, 5112 (1977).

Tsurutani, B. T., and P. Rodriguez, Upstream Waves and Particles: An Overview of ISEE Results, *J. Geophys. Res.*, **86**, 4319 (1981).

Tsurutani, B. T., E. J. Smith, R. R. Anderson, K. W. Ogilvie, J. D. Scudder, D. N. Baker, and S. J. Bame, Lion Roars and Nonoscillatory Drift Mirror Waves in the Magnetosheath, *J. Geophys. Res.*, **87**, 6060 (1982).

Tsurutani, B. T., E. J. Smith, and D. E. Jones, Waves Observed Upstream of Interplanetary Shocks, *J. Geophys. Res.*, **88**, 5645 (1983).

Tsurutani, B. T., and E. J. Smith, Magnetosonic Waves Adjacent to the Plasma Sheet in the Distant Magnetotail: ISEE-3, *Geophys. Res. Lett.*, **11**, 331 (1984).

Tsurutani, B. T., I. G. Richardson, R. M. Thorne, W. Butler, E. J. Smith, S. W. H. Cowley, S. P. Gary, S.-I. Akasofu, and R. D. Zwickl, Observations of the Right-Hand Resonant Ion Beam Instability in the Distant Plasma Sheet Boundary Layer, *J. Geophys. Res.*, **90**, 12159 (1985).

Tsurutani, B. T., D. J. Southwood, E. J. Smith, and A. Balogh, A Survey of Low Frequency Waves at Jupiter: The Ulysses Encounter, *J. Geophys. Res.*, **98**, 21203 (1993).

Tsurutani, B. T., and G. S. Lakhina, Some Basic Concepts of Wave-Particle Interactions in Collisionless Plasmas, *Rev. Geophys.*, **35**, 491 (1997).

Zwan, B. J., and R. A. Wolf, Depletion of the Solar Wind Plasma Near a Planetary Boundary, *J. Geophys. Res.*, **81**, 1636 (1976).

Zhang, Y., H. Matsumoto, and H. Kojima, Lion Roars in the Magnetosheath: GEOTAIL Observations, *J. Geophys. Res.*, **103**, 4615 (1998).

Table 1. Foreshock Waves. Day 230, 1999.

	Start Time	Stop Time	T	|B|	λ_1/λ_2	θ_{KB}	Polarization
1	1:51:00.2	1:51:00.6	0.4	8	17.5	32	RH
2	1:51:00.7	1:51:00.9	0.2	8	1.9	69	RH
3	1:51:01.9	1:51:02.5	0.6	9	1.4	25	RH
4	1:51:02.5	1:51:03.7	1.2	9	1.3	44	RH
5	1:51:03.7	1:51:05.0	1.3	9	1.9	21	RH
6	1:51:05.0	1:51:05.6	0.6	9	3.7	35	RH
7	1:51:05.6	1:51:06.4	0.8	8	3.0	18	RH
8	1:51:06.7	1:51:07.3	0.6	8	1.7	60	LH
9	1:51:07.3	1:51:07.8	0.5	8	3.7	22	RH
10	1:51:07.8	1:51:08.2	0.4	8	7.3	11	RH
11	1:51:08.2	1:51:08.7	0.5	8	2.0	72	RH
12	1:51:08.8	1:51:09.3	0.5	9	4.3	28	RH
13	1:51:09.3	1:51:10.0	0.7	9	5.1	32	RH
14	1:51:10.2	1:51:10.7	0.5	8	5.0	79	LH
15	1:51:10.8	1:51:11.5	0.7	8	8.5	15	RH
16	1:51:11.6	1:51:12.0	0.4	8	3.0	47	RH
17	1:51:12.0	1:51:12.5	0.5	10	2.1	55	RH
18	1:51:12.5	1:51:13.2	0.7	9	3.3	39	RH
19	1:51:13.2	1:51:13.8	0.6	9	2.7	6	RH
20	1:51:13.8	1:51:14.6	0.8	8	3.5	86	RH
21	1:51:14.7	1:51:15.2	0.5	9	7.3	62	linear
22	1:51:15.3	1:51:16.5	1.2	10	4.6	46	RH
23	1:51:16.6	1:51:17.4	0.8	10	1.9	8	RH
24	1:51:17.5	1:51:18.7	1.2	8	2.9	15	RH
25	1:51:18.7	1:51:19.5	0.8	8	2.1	27	RH
26	1:51:19.5	1:51:20.3	0.8	8	3.1	17	RH
27	1:51:20.3	1:51:21.3	1.0	9	4.5	50	RH
28	1:51:21.2	1:51:21.9	0.7	10	2.6	25	RH
29	1:51:22.0	1:51:23.0	1.0	10	2.8	9	RH
30	1:51:23.0	1:51:23.5	0.5	8	4.4	67	RH
31	1:51:23.6	1:51:24.2	0.6	8	3.1	14	RH
32	1:51:24.2	1:51:25.1	0.9	9	3.0	18	RH
33	1:51:25.1	1:51:26.4	1.3	10	7.5	50	linear
34	1:51:26.5	1:51:27.4	0.9	8	2.7	37	RH
35	1:51:27.4	1:51:27.8	0.4	7	5.6	72	LH
36	1:51:27.9	1:51:28.8	0.9	8	1.4	85	LH
37	1:51:28.8	1:51:29.3	0.5	8	4.7	43	RH
38	1:51:29.2	1:51:30.5	1.3	15	10.3	55	RH
39	1:51:30.7	1:51:31.5	0.8	15	5.1	59	LH
40	1:51:31.5	1:51:32.3	0.8	15	2.7	50	RH
41	1:51:32.4	1:51:33.1	0.7	15	4.5	64	RH
42	1:51:33.1	1:51:33.8	0.7	15	7.4	59	linear
43	1:51:33.8	1:51:34.3	0.5	15	2.2	27	RH
44	1:51:34.3	1:51:34.9	0.6	15	2.1	64	RH
45	1:51:34.9	1:51:35.3	0.4	15	1.5	50	RH
46	1:51:35.3	1:51:36.1	0.8	15	8.2	51	RH
47	1:51:36.1	1:51:36.6	0.5	15	3.3	56	RH
48	1:51:36.8	1:51:37.1	0.3	15	7.8	44	RH
49	1:51:37.2	1:51:37.8	0.6	15	8.2	26	RH
50	1:51:37.9	1:51:38.6	0.7	15	1.3	59	RH
51	1:51:38.6	1:51:39.2	0.6	15	3.8	66	linear
52	1:51:39.5	1:51:39.8	0.3	15	2.4	20	RH
53	1:51:39.9	1:51:40.6	0.7	15	2.0	52	RH

54	1:51:40.7	1:51:41.4	0.7	15	1.8	38	RH
55	1:51:41.5	1:51:41.9	0.4	15	12.2	80	linear
56	1:51:41.9	1:51:42.5	0.6	15	3.3	88	RH
57	1:51:42.5	1:51:42.8	0.3	15	1.7	36	RH
58	1:51:42.8	1:51:43.2	0.4	15	1.6	77	RH
59	1:51:43.2	1:51:44.1	0.9	15	2.7	87	linear
60	1:51:44.1	1:51:44.8	0.7	25	8.4	76	RH
61	1:51:44.8	1:51:45.3	0.5	20	2.2	77	RH
62	1:51:45.4	1:51:45.9	0.5	20	2.7	52	LH
63	1:51:46.0	1:51:46.7	0.7	20	3.0	46	RH
64	1:51:46.8	1:51:47.1	0.3	30	4.3	53	RH
65	1:51:47.4	1:51:48.1	0.7	35	6.6	15	RH
66	1:51:48.2	1:51:48.6	0.4	35	8.2	19	RH
67	1:51:49.2	1:51:49.7	0.5	35	192.4	81	-

Table 2. Magnetosheath Waves. Day 230, 1999.

	Start Time	Stop Time	T	|B|	λ_1/λ_2	θ_{KB}	Polarization
1	1:52:02.6	1:52:17.4	3.7	25	1.8	72	-
	1:52:02.6	1:52:06.6	-	-	16.9	71	linear
	1:52:06.6	1:52:09.8	-	-	3.4	73	-
	1:52:09.8	1:52:12.9	-	-	4.1	52	LH
	1:52:12.9	1:52:17.4	-	-	1.4	70	LH
2	1:54:07.8	1:54:20.7	4.3	27	1.9	32	LH
	1:54:07.8	1:54:12.2	-	-	11.6	56	LH
	1:54:12.2	1:54:16.1	-	-	1.5	31	LH
	1:54:16.2	1:54:20.7	-	-	5.1	50	LH
3	1:57:03.1	1:57:24.4	5.3	31	2.0	15	LH
	1:57:03.1	1:57:07.7	-	-	2.6	6	LH
	1:57:07.8	1:57:12.9	-	-	4.0	13	LH
	1:57:13.0	1:57:18.8	-	-	5.1	18	LH
	1:57:18.9	1:57:24.4	-	-	11.1	31	LH elliptical
4	2:01:22.9	2:01:45.4	5.6	32	3.2	24	LH
	2:01:22.9	2:01:28.7	-	-	4.5	3	LH
	2:01:28.7	2:01:34.4	-	-	4.0	49	LH
	2:01:34.4	2:01:39.3	-	-	10.8	79	LH
	2:01:39.4	2:01:45.4	-	-	3.0	16	LH
5	2:04:10.3	2:04.33.8	5.9	31	1.3	11	LH
	2:04:10.3	2:04:16.5	-	-	7.2	11	LH
	2:04:16.5	2:04:21.3	-	-	3.5	37	LH
	2:04:21.6	2:04:27.0	-	-	5.6	28	LH
	2:04:27.0	2:04:33.8	-	-	2.2	9	LH
6	2:05:06.2	2:05:29.2	5.8	33	2.8	32	-
	2:05:06.2	2:05:10.9	-	-	2.0	45	LH
	2:05:10.9	2:05:15.5	-	-	5.3	42	LH
	2:05:15.5	2:05:21.3	-	-	3.0	75	RH
	2:05:21.6	2:05:29.2	-	-	1.4	10	RH
7	2:05:29.4	2:05:55.0	6.4	35	2.1	6	LH
	2:05:29.4	2:05:36.1	-	-	1.7	28	LH
	2:05:36.1	2:05:41.9	-	-	2.1	56	LH
	2:05:41:9	2:05:48.6	-	-	4.9	12	LH
	2:05:48.6	2:05:55.0	-	-	1.8	78	LH
8	2:05:55.0	2:06:21.2	5.2	32	1.9	15	LH
	2:05:55.0	2:06:00.0	-	-	3.5	14	LH
	2:06:00.0	2:06:06.3	-	-	2.4	20	LH
	2:06:06.3	2:06:11.1	-	-	8.5	32	LH
	2:06:11.1	2:06:16.4	-	-	9.9	81	linear
	2:06:16.4	2:06:21.2	-	-	2.0	31	LH
9	2:06:21.2	2:06:48.7	6.9	34	1.8	12	LH
	2:06:21.2	2:06:27.8	-	-	2.3	84	LH
	2:06:35.4	2:06:42.5	-	-	1.7	19	LH
	2:06:42.5	2:06:48.7	-	-	1.6	9	LH
10	2:06:48.7	2:07:17.0	7.1	35	1.2	30	LH
	2:06:48.7	2:06:56.6	-	-	2.3	24	linear
	2:06:56.6	2:07:04.4	-	-	2.4	50	LH
	2:07:04.4	2:07:11.6	-	-	1.4	11	LH/linear
	2:07:11.6	2:07:17.0	-	-	1.8	13	LH
11	2:07:17.0	2:07:37.6	6.9	35	3.3	15	LH
	2:07:17.0	2:07:22.8	-	-	4.1	63	LH
	2:07:22.8	2:07:29.8	-	-	3.8	80	LH
	2:07:29.8	2:07:37.6	-	-	1.3	7	LH

12	2:07:37.6	2:07:58.5	7.0	35	2.7	90	-
	2:07:37.6	2:07:44.2	-	-	2.0	50	LH
	2:07:44.2	2:07:50.7	-	-	2.1	77	linear
	2:07:50.7	2:07:58.5	-	-	6.2	69	linear
13	2:07:58.5	2:08:24.7	6.6	35	1.1	26	LH
	2:07:58.5	2:08:03.7	-	-	7.0	48	LH
	2:08:03.7	2:08:10.2	-	-	1.9	9	linear
	2:08:10.2	2:08:18.0	-	-	2.2	34	LH
	2:08:18.0	2:08:24.7	-	-	2.7	79	LH
14	2:08:24.7	2:08:49.7	5.0	34	2.3	52	LH
	2:08:24.7	2:08:28.9	-	-	5.2	69	LH
	2:08:28.9	2:08:33.1	-	-	4.7	27	LH
	2:08:33.1	2:08:39.8	-	-	1.7	44	LH
	2:08:39.8	2:08:44.1	-	-	4.9	60	linear
	2:08:44.2	2:08:49.7	-	-	11.5	43	LH/elliptical
15	2:08:49.7	2:09:17.5	6.9	35	1.7	52	-
	2:08:49.7	2:08:53.6	-	-	2.6	60	linear
	2:08:53.6	2:09:05.3	-	-	1.3	64	LH
	2:09:05.6	2:09:11.8	-	-	4.5	61	LH
	2:09:11.8	2:09:17.5	-	-	3.4	78	RH
16	2:09:17.5	2:09:39.0	7.2	35	2.1	63	-
	2:09:17.5	2:09:24.7	-	-	3.1	65	RH
	2:09:25.3	2:09:30.0	-	-	2.9	31	LH
	2:09:30.0	2:09:39.0	-	-	3.9	32	LH
17	2:09:39.0	2:10:01.5	7.5	35	2.7	50	LH
	2:09:39.0	2:09:47.6	-	-	2.9	42	-
	2:09:47.6	2:09:56.5	-	-	3.8	81	LH
	2:09:56.5	2:10:01.5	-	-	1.4	40	LH
18	2:12:27.1	2:12:45.5	6.1	36	2.7	11	LH
	2:12:27.1	2:12:32.7	-	-	8.9	35	LH
	2:12:32.7	2:12:37.9	-	-	6.1	66	RH
	2:12:37.9	2:12:45.5	-	-	1.6	35	LH
19	2:20:18.3	2:20:31.5	4.4	46	5.0	2	LH
	2:20:18.3	2:20:22.2	-	-	1.8	14	LH
	2:20:22.2	2:20:25.7	-	-	2.7	9	LH
	2:20:25.7	2:20:31.5	-	-	33.0	1	LH

Table 3. Magnetospheric Waves. Day 230, 1999.

	Start Time	Stop Time	T	|B|	λ_1/λ_2	θ_{KB}	Polarization
1	2:29:15.2	2:29:18.3	1.5	63	1.9	29	LH
	2:29:15.2	2:29:16.7	-	-	3.4	32	LH
	2:29:16.7	2:29:18.3	-	-	1.6	26	LH
2	2:31:27.1	2:31:33.9	2.3	60.7	4.0	7	LH
	2:31:27.1	2:31:29.3	-	-	1.5	13	LH
	2:31:29.3	2:31:31.6	-	-	27.1	18	LH
	2:31:31.6	2:31:33.9	-	-	8.3	7	LH
3	2:32:29.9	2:32:46.1	2.7	61.4	5.5	41	linear
	2:32:29.9	2:32:32.7	-	-	20.2	23	LH elliptical
	2:32:32.7	2:32:35.4	-	-	42.9	17	LH elliptical
	2:32:35.5	2:32:38.1	-	-	174.8	62	linear
	2:32:38.2	2:32:41.1	-	-	106.4	37	linear
	2:32:41.1	2:32:43.6	-	-	24.7	71	LH elliptical
	2:32:43.6	2:32:46.1	-	-	21.4	20	linear
4	2:33:40.0	2:33:51.1	2.8	63.6	1.6	21	LH
	2:33:40.0	2:33:42.7	-	-	5.2	18	LH
	2:33:42.8	2:33:45.2	-	-	2.7	31	LH
	2:33:45.3	2:33:48.0	-	-	2.5	23	LH
	2:33:48.1	2:33:51.1	-	-	2.4	23	LH
5	2:37:30.5	2:37:43.4	2.6	69.1	2.9	9	LH
	2:37:30.5	2:37:33.3	-	-	2.5	6	LH
	2:37:33.5	2:37:35.8	-	-	4.0	10	LH
	2:37:35.8	2:37:38.1	-	-	2.8	10	LH
	2:37:38.1	2:37:40.8	-	-	9.5	13	LH
	2:37:40.8	2:37:43.4	-	-	10.0	17	linear